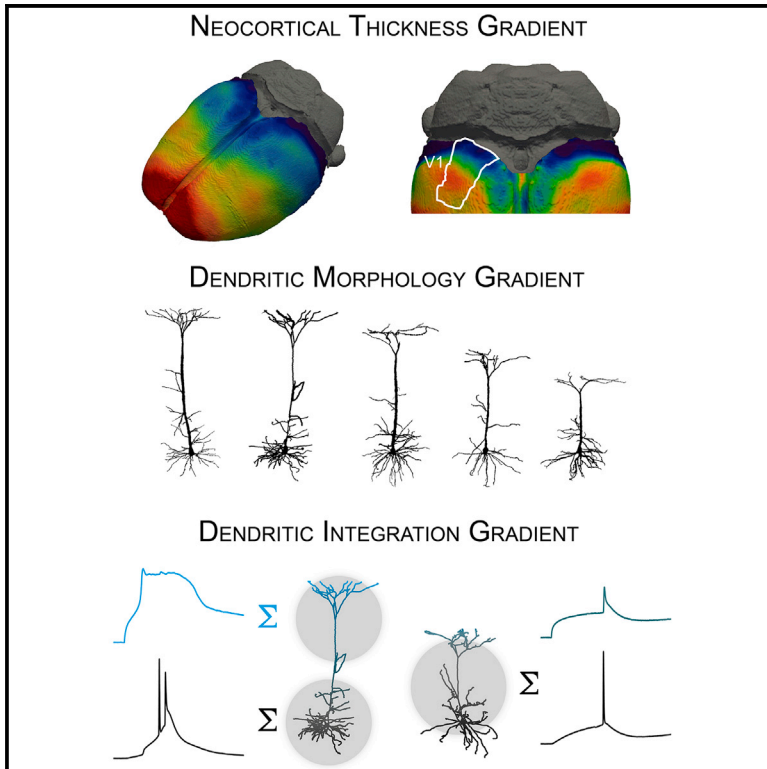


Neocortical Topology Governs the Dendritic Integrative Capacity of Layer 5 Pyramidal Neurons

Graphical Abstract



Authors

Lee N. Fletcher, Stephen R. Williams

Correspondence

srw@uq.edu.au

In Brief

Fletcher and Williams demonstrate that neuronal computations are determined by neocortical location. Dendritic integration in the primary visual cortex is governed by neuronal morphology and biophysics, creating a gradient of information processing that challenges the idea of stereotyped microcircuit operation.

Highlights

- Neocortical thickness varies as a gradient across the rat primary visual cortex
- Neocortical structure governs apical dendritic morphology of V1 principal neurons
- Principal neurons exhibit a gradient of dendritic information processing across V1
- Neocortical structure and biophysics enforce a computational gradient across V1



Neocortical Topology Governs the Dendritic Integrative Capacity of Layer 5 Pyramidal Neurons

Lee N. Fletcher¹ and Stephen R. Williams^{1,2,*}

¹Queensland Brain Institute, The University of Queensland, Brisbane, QLD 4072, Australia

²Lead Contact

*Correspondence: srw@uq.edu.au

<https://doi.org/10.1016/j.neuron.2018.10.048>

SUMMARY

The structure of the neocortex varies across the neocortical mantle to govern the physical size of principal neurons. What impact such anatomical variation has on the computational operations of principal neurons remains unknown. Here, we demonstrate within a functionally defined area that neocortical thickness governs the anatomical, electrophysiological, and computational properties of the principal output neurons of the neocortex. We find that neocortical thickness and the size of layer 5B pyramidal neurons changes as a gradient across the rostro-caudal axis of the rat primary visual cortex. Simultaneous somato-dendritic whole-cell recordings and compartmental modeling revealed that the electrical architecture of principal neurons was not preserved; rather, primary visual cortex site-dependent differences in intracellular resistivity accentuated a gradient of the electrical behavior of layer 5B pyramidal neurons to influence the emergence of active dendritic computations. Our findings therefore reveal an exquisite relationship between neocortical structure and neuronal computation.

INTRODUCTION

A key problem in neuroscience is to understand how circuit-based computations are implemented in the brain (van Hemmen and Sejnowski, 2006). Recent work has shown that active dendritic integration plays a central role in circuit-based computations in retinal, hippocampal, and neocortical networks, where principal neurons do not operate as simple point processors but function as multilayered integrators of dendritic synaptic input (Bittner et al., 2015; Harnett et al., 2013; Larkum et al., 2009; Losonczy et al., 2008; Poirazi et al., 2003; Polsky et al., 2004; Sivyer and Williams, 2013; Smith et al., 2013; Takahashi et al., 2016; Xu et al., 2012).

In the neocortex, a general model for the multilayered integrative and computational operations of the major subcortical projection neurons, layer 5B (L5B) pyramidal neurons, has been derived from recordings made principally from the primary somatosensory cortex (Larkum, 2013; Stuart and Spruston,

2015). At thin, terminal dendritic branches, excitatory synaptic input is nonlinearly integrated through NMDA-receptor-mediated mechanisms (Branco and Häusser, 2010; Harnett et al., 2013; Larkum et al., 2009; Polsky et al., 2004; Schiller et al., 2000). The results of such local computations in terminal dendrites of the apical dendritic tuft are, in turn, integrated at distal apical dendritic trunk sites by the recruitment of voltage-activated ion channels, leading to the generation of dendritic spikes (Larkum et al., 1999; Williams and Stuart, 2002; Xu et al., 2012). The resultant apical dendritic trunk spikes forward-propagate to the final site of integration, the proximal axon, where action potential (AP) output is initiated. This model is bi-directional, allowing higher and lower layers to nonlinearly interact (Harnett et al., 2013; Larkum et al., 1999; Williams, 2005; Xu et al., 2012). At the foundation of such integration schemes lies the spatially distributed morphology of neurons, which together with the passive biophysical properties represent a framework upon which single neuron computations are built (Stuart and Spruston, 1998; Vetter et al., 2001; Zador et al., 1995).

The thickness of the mammalian neocortex is, however, not constant and varies across the mantle (Cahalane et al., 2012; Glasser et al., 2016; Rockel et al., 1980) to govern the size of principal neurons. In order for neuronal circuits to carry out canonical computations (Douglas and Martin, 2004; Harris and Shepherd, 2015; Markram et al., 2015), it is critical the integrative properties of single neocortical neurons are preserved despite pronounced morphological variation. Here, we directly investigate the impact that neocortical structure has on the integrative and computational properties of L5B pyramidal neurons of the rat primary visual cortex (V1).

RESULTS

Neocortical Thickness Defines the Apical Dendritic Arborization of L5B Pyramidal Neurons

Structural magnetic resonance imaging (MRI) revealed that the thickness of the rat neocortex exhibited a 3-fold range across the neocortical mantle (Figures 1A and S1; ~1 to ~3 mm, measured as the perpendicular distance from the pia to the subcortical white matter; 50 μ m resolution; n = 5 registered brains), consistent with histological analysis (Paxinos and Watson, 2007). Within the primary visual cortex, a rapid gradient of neocortical thickness was apparent (Figures 1B–1E). This gradient ran rostro-caudally, in line with the long axis of V1 (Figure 1C). The thickness of the neocortex was greatest in rostral V1

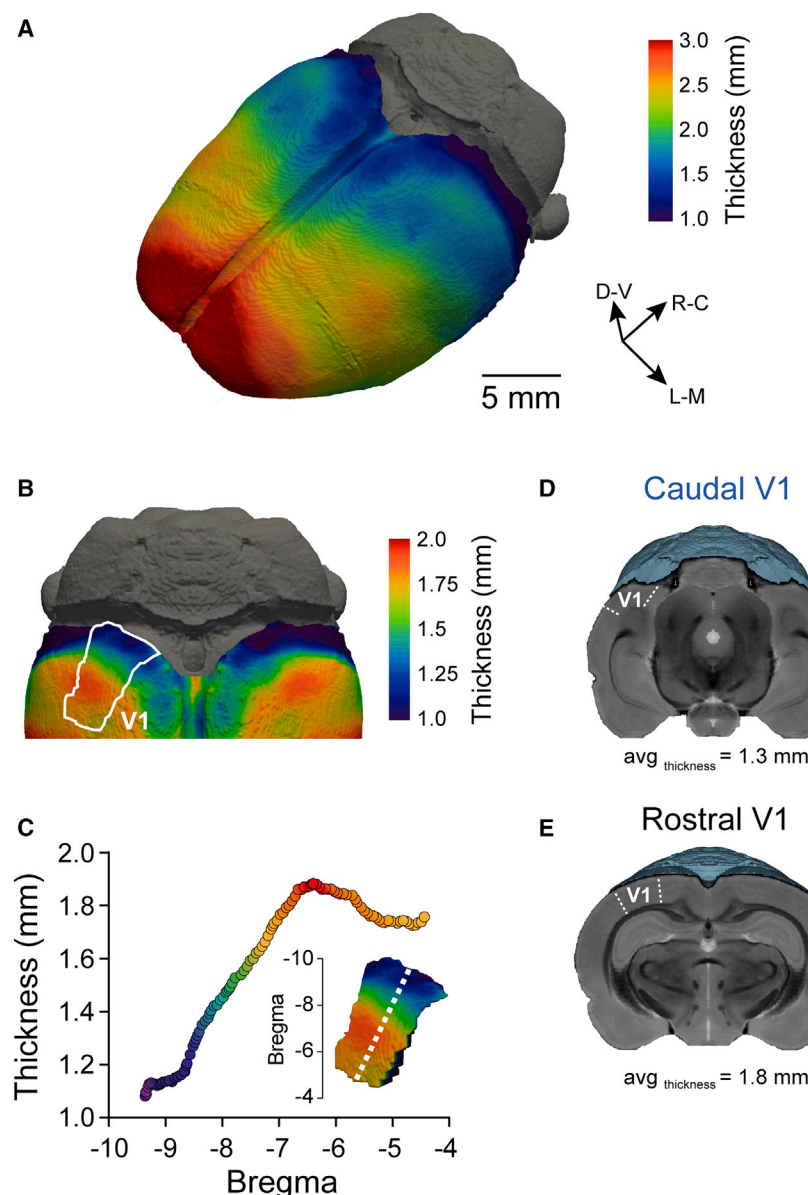


Figure 1. The Thickness of the Primary Visual Cortex Is Not Uniform

(A) Topography of neocortical thickness. The direction of the dorsal-ventral (D-V) axis, rostral-caudal (R-C) axis, and medial-lateral (L-M) axis is indicated.

(B) Variation of neocortical thickness is apparent within the primary visual cortex (V1). V1 is outlined in white and delineated with reference to a rat brain atlas. Note the change in the color axis scale from (A).

(C) Gradation of neocortical thickness across V1 aligned to the long axis of V1 (white dotted line). Color is coded according to the scale in (B).

(D and E) Virtual slicing of MRI images at angles at which caudal (D) and rostral (E) V1 brain slices were prepared for electrophysiological recordings and morphological analysis.

See also Figure S1.

(maximum 1.90 mm), transitioned to a minimum at the caudal pole (minimum 0.97 mm), and was similar between hemispheres when determined both algorithmically (Figure 1C) and manually (Figures 1D and 1E; left V1: rostral = 1.70 mm, caudal = 1.39 mm; right V1: rostral = 1.71 mm, caudal = 1.36 mm). In contrast, considerably less variation was apparent across the medial-lateral axis of V1 (Figure S1; rostral = 1.79–1.90 mm; caudal = 0.97–1.26 mm).

The morphology of the apical dendritic tree of L5B neurons changed considerably across the longitudinal rostral-caudal axis of V1 (Figures 2A and 2B). Anatomical reconstruction of biocytin-filled neurons, recorded in acute brain slices of V1, revealed that the morphology of L5B pyramidal neurons was dominated by a large apical dendritic trunk that branched into an extensive tuft in layer 1 (Figure 2A). Across the rostral-caudal

axis of V1, the average path length from the soma to the termini of apical tuft dendrites linearly decreased (Figure 2D; range = 584–1,108 μm ; linear regression: slope = 68.0 $\mu\text{m}/\text{mm}$ of bregma, $r = 0.71$, $F = 98.2$, $n = 97$, $p < 0.0001$). This relationship was formed by a change in apical trunk path length, as no gradient of the path length of apical dendritic tuft dendrites was observed (Figures 2E and S2A; trunk path length measured from the soma to the base of the tuft: range = 354–882 μm ; linear regression; slope = 63.6 $\mu\text{m}/\text{mm}$ of bregma, $r = 0.71$, $F = 98.4$, $n = 97$, $p < 0.0001$; average tuft path length measured from the base to the termini of apical dendritic tuft dendrites: $F = 0.81$, $n = 97$, $p = 0.371$). Notably, this rostral-caudal gradient was unaccompanied by differences in the diameter of the apical dendritic trunk or the branching complexity and field volume of the apical dendritic tuft (Figures S2 and S3). Furthermore, oblique dendrites, which decorated the proximal apical dendritic trunk, did not change in size across V1, although there

was a positive correlation with the apical trunk length (Figure S2). Similarly, the volume and total length of the basal dendritic tree did not differ across V1 (Figures 2C and S2). A correlation was, however, apparent between soma volume and rostral-caudal position (Figure S2).

Importantly, retrograde tracer injections revealed that the rostral-caudal gradient of apical dendritic morphology was indistinguishable for L5B pyramidal neurons projecting to an identified subcortical target, the superior colliculus (Figures 2D–2F; red symbols represent superior-colliculi projecting L5B pyramidal neurons). Taken together, these findings indicate that a gradient of neocortical thickness across V1 governs the apical dendritic trunk length of L5B pyramidal neurons, defining the physical distance that separates the apical tuft from the rest of the neuron.

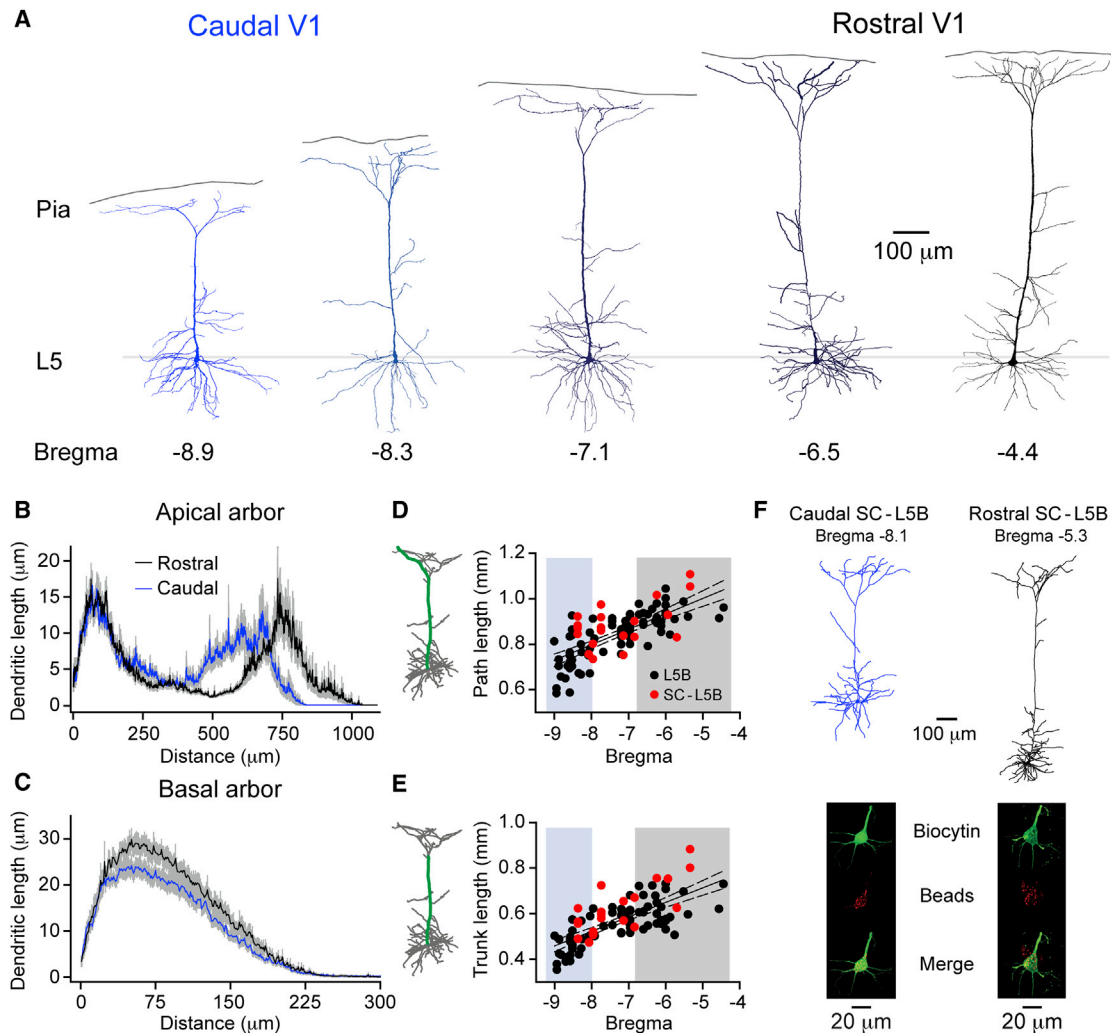


Figure 2. Rostro-caudal Gradient of Apical Dendritic Morphology across the Primary Visual Cortex

(A) Layer 5B pyramidal neurons reconstructed from brain slices of V1.

(B and C) Quantification of apical (B) and basal (C) dendritic lengths of layer 5B (L5B) pyramidal neurons ($n = 97$) as a function of the radial distance from the soma (mean \pm SEM, 1- μm bins). The divisions between rostral and caudal correspond to cortical locations that delineate the thinnest and thickest plateau regions of neocortical thickness (shaded regions in D).

(D) Average soma to distal apical tuft termini path length in L5B pyramidal neurons positively correlates with cortical position. Neurons co-labeled by the transport of retrobeads from the superior colliculus (SC) are red ($n = 20$). The solid and dotted lines indicate a linear regression and 95% confidence intervals, respectively.

(E) Apical dendrite trunk length positively correlates with cortical position.

(F) Reconstruction of SC targeting L5B pyramidal neurons labeled by retrobeads (red), following biocytin filling (green).

See also [Figures S2](#) and [S3](#).

Functional Impact of the Rostro-caudal Gradient of Apical Dendritic Morphology

In order to test if the rostro-caudal gradient of apical dendritic morphology impacts the integrative operations of V1 L5B pyramidal neurons, we made simultaneous triple current-clamp whole-cell recordings from the soma and distal apical dendritic sites. All dendritic recordings were made at the base of the apical dendritic tuft using closely spaced electrodes to independently inject current and record voltage ([Figures 3A, 3B, and S4A](#); apical dendritic trunk length = $550.9 \pm 10.4 \mu\text{m}$; dendritic recording distance from soma = $527.1 \pm 10.9 \mu\text{m}$; $n = 125$; dendritic elec-

trode separation = $10.7 \pm 1.1 \mu\text{m}$). We first analyzed the somatic impact of dendritic voltage responses generated by long steps of negative current ([Figures 3A and 3B](#); peak dendritic voltage response = $-20.1 \pm 0.1 \text{ mV}$, dendritic current = $-0.68 \pm 0.02 \text{ nA}$, duration = 600 ms). In caudal V1 L5B pyramidal neurons a considerable proportion of voltage spread from the dendritic site of generation to the soma, whereas in rostral V1 neurons, only a small fraction of voltage was recorded from the soma at peak and steady state ([Figures 3A and 3B](#)). Analysis across the rostro-caudal axis of V1 revealed that the fraction of voltage reaching the soma declined as the length of the apical dendritic

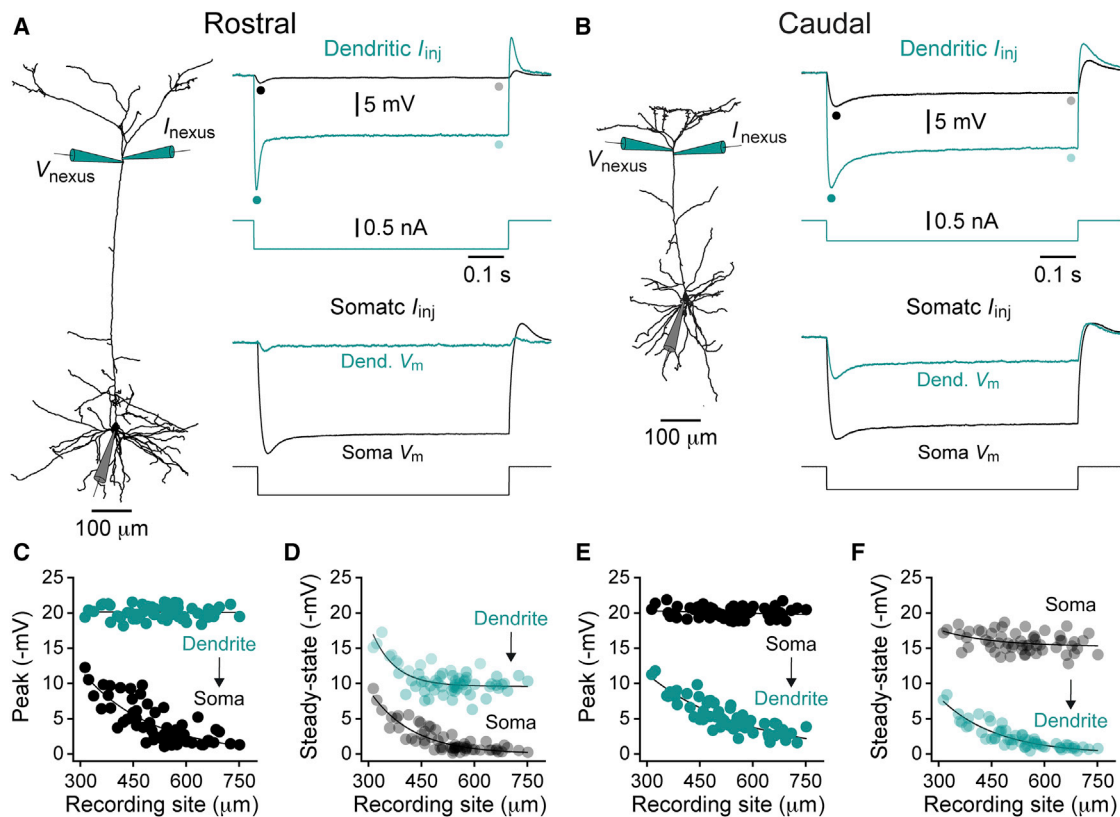


Figure 3. Rostro-caudal Gradient of Apical Dendritic Voltage Attenuation

(A and B) Voltage attenuation in the apical dendritic tree of rostral (A) and caudal (B) V1 L5B pyramidal neurons. Overlain voltage responses simultaneously recorded from distal apical dendritic (green traces, Dend. V_m) and somatic (black traces, Soma V_m) sites in response to the indicated steps of somatic or dendritic current (I_{inj}). The morphology of recorded neurons and placement of recording electrodes are shown.

(C–F) Measurement of the local and dendritic trunk-length-dependent attenuation of voltage responses at peak amplitude (C and E) and steady state (D and F). Solid lines represent single exponential fits to the data. All dendritic recordings were made at sites close to the nexus of the apical dendritic trunk (distance from nexus = $22.1 \pm 2.6 \mu\text{m}$, $n = 61$).

See also Figure S4.

trunk increased, a relationship that could be fit with an exponential function (Figures 3C, 3D, and S4B; 50% voltage transfer = $334 \mu\text{m}$). A similar relationship was found for the somato-dendritic spread of voltage signals (Figures 3E, 3F, and S4B; peak somatic voltage response = $-19.9 \pm 0.1 \text{ mV}$, somatic current = $-0.76 \pm 0.03 \text{ nA}$; 50% voltage transfer = $330 \mu\text{m}$). These data indicate that the electrical architecture of L5B pyramidal neurons is not preserved across the rostro-caudal axis of V1 and suggest that the electrical compactness of caudal L5B pyramidal neurons may limit the expression of multilayered active dendritic integration, a functional hallmark of L5B pyramidal neurons (Larkum, 2013; Stuart and Spruston, 2015).

In order to test this idea, we injected rheobase-positive current steps at distal apical dendritic recording sites. In rostral L5B pyramidal neurons, dendritic current steps evoked large-amplitude apical dendritic spikes (Figure 4A). In contrast, in caudal L5B pyramidal neurons, dendritic current steps did not generate dendritic spikes; rather, voltage spread directly from the dendritic site of generation to the soma and axon to initiate AP firing (Figure 4A). Analysis of the time interval between the detection of

regenerative spikes at dendritic and somatic recording sites revealed an apical dendritic trunk-length-dependent bifurcation (Figure 4B). In caudal L5B pyramidal neurons, with apical dendritic trunks $<480 \mu\text{m}$, dendritic excitation typically directly evoked AP firing (40 of 48 neurons), whereas in larger rostral neurons, dendritic spikes preceded and drove AP output (Figure 4B; $>550 \mu\text{m}$, 49 of 49 neurons). In contrast, when rheobase-positive current steps were injected at the soma, a simple monotonic distance-dependent relationship was found as APs back-propagated to the dendritic recording site (Figure 4C).

To explore if this bifurcation of dendritic integrative behavior was also apparent in response to more physiological patterns of dendritic excitatory input, we utilized microiontophoresis techniques to drive dendritic excitation through the activation of glutamate-receptor-mediated mechanisms (Müller et al., 2012). Consistent with results obtained using dendritic current steps, we found that the brief and local apical dendritic iontophoretic application of glutamate evoked fast excitatory responses leading to the powerful generation of dendritic spikes in rostral L5B pyramidal neurons (Figures 4D and S5A–S5C; distance

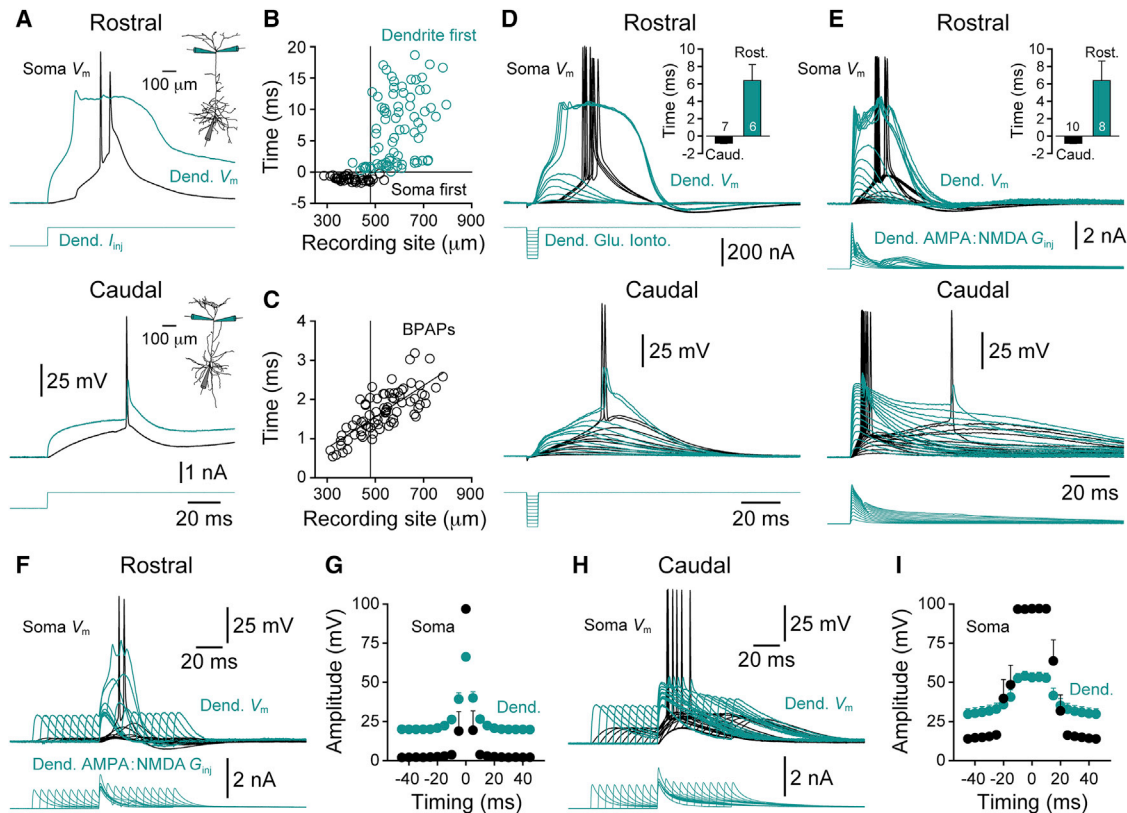


Figure 4. Differential Expression of Active Dendritic Integration in Rostral and Caudal Layer 5B Pyramidal Neurons

(A) Rheobase-positive current steps drive dendritic spike initiation in rostral, but not caudal, V1 L5B pyramidal neurons. Insets show neuronal morphology and the placement of recording electrodes.

(B) Time delay between regenerative spikes recorded at dendritic and somatic sites. Dendritic electrodes were positioned close to the base of the apical dendritic tuft (distance from nexus = $23.7 \pm 2.1 \mu\text{m}$, $n = 124$). Dendritic spike initiation preceded AP firing in recordings illustrated by green symbols.

(C) Back-propagating action potentials (BPAPs) invaded the apical dendritic tree with a monotonic distance-dependent relationship (solid line, linear regression).

(D) Apical dendritic iontophoretic glutamate application drives dendritic spike initiation in rostral (upper voltage traces), but not caudal (lower voltage traces), V1 L5B pyramidal neurons.

(E) Injection of apical dendritic excitatory conductance drives dendritic spike initiation in rostral, but not caudal V1 L5B pyramidal neurons. The insets in (D) and (E) show the time delay (mean \pm SEM) between regenerative spikes recorded at dendritic and somatic sites.

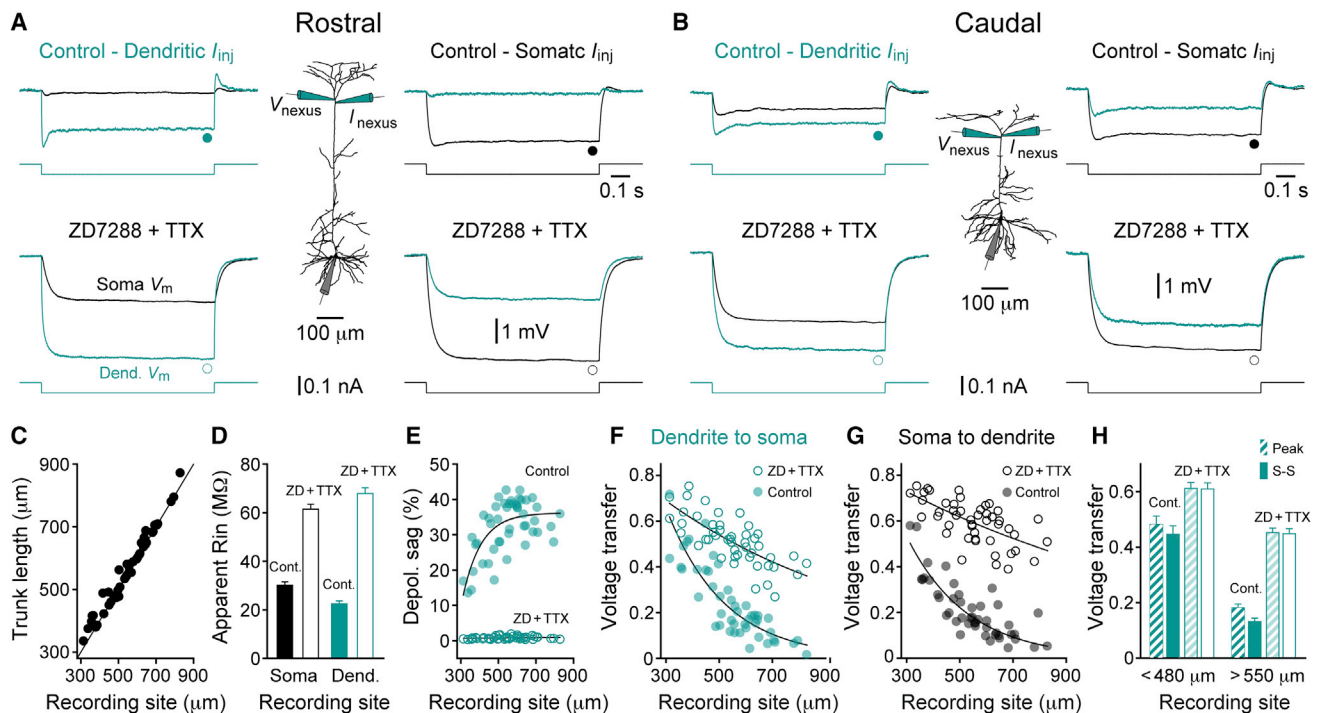
(F and H) Rostral (F) and caudal (H) V1 L5B pyramidal neurons show distinct modes and time windows of integration in response to distal apical dendritic injection of pairs of simulated AMPA:NMDA-receptor-mediated excitatory postsynaptic conductance changes. The rostral neuron generated dendritic-spike-driven AP firing only during coincident presentation (separation 0 to ± 45 ms [in 5-ms steps]). In contrast, the injection of dendritic excitatory conductance in the caudal neuron directly evoked AP firing across a wide time window.

(G and I) Pooled data showing the average (\pm SEM) somatic (black) and dendritic (green) peak voltage response evoked by distal apical dendritic excitatory conductance generated at the indicated time intervals in rostral (G) and caudal (I) L5B pyramidal neurons.

from soma = $585.1 \pm 26.1 \mu\text{m}$, $n = 6$). In contrast, in caudal neurons, glutamate-evoked dendritic excitatory responses did not evoke dendritic electrogenesis; instead, voltage spread to the soma and axon to directly drive AP firing (Figure 4D, Figures S5A–S5C; distance from soma = $387.0 \pm 18.8 \mu\text{m}$, $n = 7$). Furthermore, in response to the generation of families of simulated dual-component AMPA:NMDA-receptor-mediated excitatory postsynaptic potentials (EPSPs), generated using dendritic dynamic-clamp techniques (Harnett et al., 2015), a dendritic spike was initiated as a threshold response in rostral neurons and throughout a wide supra-threshold range (Figure 4E; distance from soma = $644.0 \pm 25.0 \mu\text{m}$, $n = 8$). In caudal neurons, however, dynamic-clamp EPSPs failed to evoke dendritic electrogenesis but directly drove AP firing across a wide supra-threshold range

(Figures 4E, S5D, and S5E; distance from soma = $383.8 \pm 6.4 \mu\text{m}$, $n = 10$). These data reveal that excitatory input to rostral L5B pyramidal neurons is locally integrated in the apical dendritic tree, whereas in caudal L5B pyramidal neurons, the integration of dendritic excitatory input occurs axo-somatically.

As previous work has indicated that synaptic integration at dendritic and axo-somatic sites occurs over distinct temporal windows (Williams and Stuart, 2002), we tested if the temporal integration of dendritic excitatory input was distinct in rostral and caudal V1 L5B pyramidal neurons. In rostral neurons, the time window for the integration of dendritic dual-component AMPA:NMDA EPSPs was vanishingly short, with neuronal output generated by only two temporally coincident EPSPs in 7 of 8 neurons (Figures 4F and 4G; dynamic-clamp EPSPs



separated in time by 0 to ± 45 ms, in 5-ms steps). This pattern of neuronal output was generated by local dendritic integration, leading to the generation of dendritic spikes that subsequently drove AP firing (Figures 4F and 4G). Conversely, caudal neurons integrated dendritic dynamic-clamp EPSPs over a longer time window and did not require input precision to elicit AP firing, which was invariably driven by the direct spread of dendritic depolarization to the axonal site of AP initiation (Figures 4H and 4I). A similar disparity of integration time windows was observed when dendritic simulated EPSPs were generated in response to ideal current sources (Figures S5F–S5I). Synaptic integration in the distal dendritic arbor of rostral V1 L5B pyramidal neurons therefore occurs locally and is operational over the fast dendritic time constant, whereas the integration of dendritic excitatory input in caudal L5B pyramidal neurons occurs over the longer axo-somatic time constant. Thus, direct recording from an anatomically common site, the base of the apical dendritic tuft, demonstrates that the electrical architecture and dendritic inte-

grative properties of L5B pyramidal neurons are not canonical in V1 but are determined by the physical size of the apical dendritic arbor.

Distinct Passive Electrical Structure of V1 L5B Pyramidal Neurons

To investigate if active conductances define the electrical architecture of rostral and caudal V1 L5B pyramidal neurons, we pharmacologically blocked the major resting conductances, mediated by hyperpolarization-activated cyclic-nucleotide-gated (HCN) channels (ZD7288, 10 μ M) and voltage-gated sodium (Na_v) channels (Tetrodotoxin, TTX, 1 μ M), which shape subthreshold voltage responses (Harnett et al., 2015; Stuart, 1999; Stuart and Spruston, 1998). Simultaneous somato-dendritic recordings demonstrated that the pharmacological reduction of resting conductance significantly increased apparent input resistance at somatic and apical dendritic recording sites and eliminated time-dependent rectification (Figures 5A–5E

and S4C; somatic [t test, $p < 0.0001$, $n = 47$] and dendritic [t test, $p < 0.0001$, $n = 47$] steady-state apparent input resistance significantly different between conditions). Notably, however, when resting conductance was pharmacologically reduced, we observed significant differences in the spread of voltage between distal apical dendritic sites and the soma of rostral and caudal L5B pyramidal neurons (Figures 5A and 5B). For comparative analysis, we divided L5B pyramidal neurons into two groups, caudal neurons (with apical trunk lengths of $<480 \mu\text{m}$) and rostral neurons (with apical trunk lengths $>550 \mu\text{m}$), a division guided by the bifurcation of dendritic integrative behavior (Figure 4). When resting conductance was reduced, a significantly greater proportion of voltage spread from distal apical dendritic sites to the soma of caudal L5B pyramidal neurons (Figures 5F and 5H; dendro-somatic voltage transfer in blockers: caudal = 0.61 ± 0.02 , $n = 14$; rostral = 0.45 ± 0.02 , $n = 24$; t test, $p < 0.0001$). The pharmacological reduction of resting conductance had a similar impact on somato-dendritic voltage transfer (Figures 5G and 5H). Together, these data indicate that rostral and caudal V1 L5B pyramidal neurons differ in their electrical architecture.

Modeling Reveals Unique Passive Biophysical Properties of Rostral and Caudal L5B Pyramidal Neurons

To explore the determinants of voltage attenuation in rostral and caudal L5B pyramidal neurons, we modeled experimental data using the NEURON simulation environment (Hines and Carnevale, 1997). Morphologically accurate, compartmental models were created ($n = 32$), and direct parameter fitting was used to determine the passive membrane properties: specific membrane resistance (R_m), specific membrane capacitance (C_m), and intracellular resistivity (R_i). Dendritic spines were not explicitly modeled but were incorporated by scaling biophysical parameters to account for additional membrane surface area (Stuart and Spruston, 1998). We fit experimental voltage responses evoked by long (-50 and -100 pA , 800 ms) and short (-2 nA , 1 ms) apical dendritic nexus current pulses recorded in the presence of antagonists of excitatory and inhibitory synaptic transmission and pharmacological blockers of resting conductance (Figure 6; ZD7288, $10 \mu\text{M}$; TTX, $1 \mu\text{M}$).

Experimentally recorded somatic and dendritic voltage responses were best described by a passive model in which R_m declined sigmoidally with distance in the apical dendritic tree, despite the pharmacological blockade of HCN channels, as previously described for L5B pyramidal neurons of the somatosensory cortex (Stuart and Spruston, 1998) (Figures 6A–6C; average error per fitted trace calculated by region fitness between experimental and simulated traces: uniform versus sigmoidal R_m ; t test, $p < 0.0001$, $n = 20$). The distribution of R_m across the apical dendritic trees of rostral and caudal neurons was similar, with both exhibiting a substantial decrease in the apical tuft (Figure 6D). The average R_m across the entire neuron was not graded across V1 (Figure 6F; $n = 32$, mean = $22.45 \pm 1.05 \text{ k}\Omega \text{ cm}^2$; linear regression with reference to apical trunk length: $F = 0.018$, $p = 0.89$). However, due to the larger size of the apical dendritic tree, rostral neurons exhibited a greater whole-cell passive conductance (Figure 6J; caudal: total

$g_{\text{passive}} = 18.97 \pm 1.28 \text{ nS}$, $n = 10$; rostral: total $g_{\text{passive}} = 53.32 \pm 11.53 \text{ nS}$, $n = 18$; Mann-Whitney test, $p < 0.0001$), which was attributable to a difference in passive apical dendritic conductance (caudal: apical dendrite $g_{\text{passive}} = 12.61 \pm 1.21 \text{ nS}$, $n = 10$; rostral: apical dendrite $g_{\text{passive}} = 44.98 \pm 11.52 \text{ nS}$, $n = 18$; Mann-Whitney test, $p < 0.0001$). The specific membrane capacitance remained relatively constant across neurons (Figure 6G; linear regression with reference to trunk length: $F = 0.1$, $p = 0.75$, mean = $1.31 \pm 0.04 \mu\text{F}/\text{cm}^2$, $n = 32$).

Surprisingly, however, direct fitting revealed that the specific intracellular resistivity of L5B pyramidal neurons showed a steep gradient across V1 (Figure 6H; linear regression with apical trunk length: slope = $13.0 \pm 3.4 \Omega \text{ cm}$ per $100 \mu\text{m}$, $r = 0.574$, $F = 14.73$, $p = 0.0006$, $n = 32$). Comparison of the average values of R_i estimated from caudal and rostral L5B pyramidal neurons revealed substantial differences (Figure 6K; caudal [apical trunk length $<480 \mu\text{m}$]: average $R_i = 47.3 \pm 4.1 \Omega \text{ cm}$, $n = 10$; rostral [apical trunk length $> 550 \mu\text{m}$]: $R_i = 88.6 \pm 6.9 \Omega \text{ cm}$, $n = 18$; t test, $p < 0.0001$). This gradient was not present when R_i was plotted against other relevant measures of morphology, suggesting a relationship specific to apical dendritic trunk length and therefore rostro-caudal position (linear regression of R_i ; average apical dendrite diameter: $r^2 = 0.11$, $p = 0.06$; total basal dendrite length: $r^2 = 0.02$, $p = 0.46$; average tuft dendrite path length: $r^2 = 0.08$, $p = 0.13$).

We next sought to gauge the impact that intracellular resistivity has on the electrical architecture of rostral and caudal L5B pyramidal neurons by determining how simulated neurons deviated from experimental data when forced with the average R_i values determined for either caudal or rostral L5B pyramidal neurons (Figures S6A and S6B; $n = 20$). Imposing the average rostral R_i onto caudal neurons caused significant errors in simulating input resistance, steady-state voltage spread, and fast voltage transients, as did imposing the average caudal R_i onto rostral neurons (Figures S6A and S6B). Thus, when fit with a range of R_i values from 5 to $200 \Omega \text{ cm}$ ($5 \Omega \text{ cm}$ steps, R_m and C_m constrained to the best fit values from nonuniform R_m model), the curves of resulting error demonstrated a shift in the values for R_i between caudal and rostral L5B neurons that produced minimum error, a difference also present when R_m was a free parameter (Figure S6C) and when C_m was constrained to $1 \mu\text{F}/\text{cm}^2$ and R_m values and shape were free to vary (Figures S6D and S6E).

In order to further explore the relationship between R_i and the rostro-caudal position of L5B pyramidal neurons in the primary visual cortex, we recorded L5B pyramidal neurons in an extracellular milieu designed to ensure that voltage responses were passive. To do so, we first recorded the dendro-somatic transfer of dendritic current-evoked voltage responses under control conditions, in the presence of blockers of excitatory and inhibitory synaptic transmission, and then in the presence of pharmacological blockers of the major resting conductance mediated by HCN and Na_v channels (ZD7288, $10 \mu\text{M}$; TTX, $1 \mu\text{M}$), and finally in the presence of these channel blockers plus a cocktail of voltage-activated ion channel antagonists (3 mM cesium, 0.1 mM barium, and 0.1 mM cadmium) designed to reduce resting conductance imparted by potassium, calcium, and classes of leak channels (Harnett et al., 2013; Losonczy et al., 2008) (Figure 7; $n = 29$). The application of this cocktail of voltage-gated

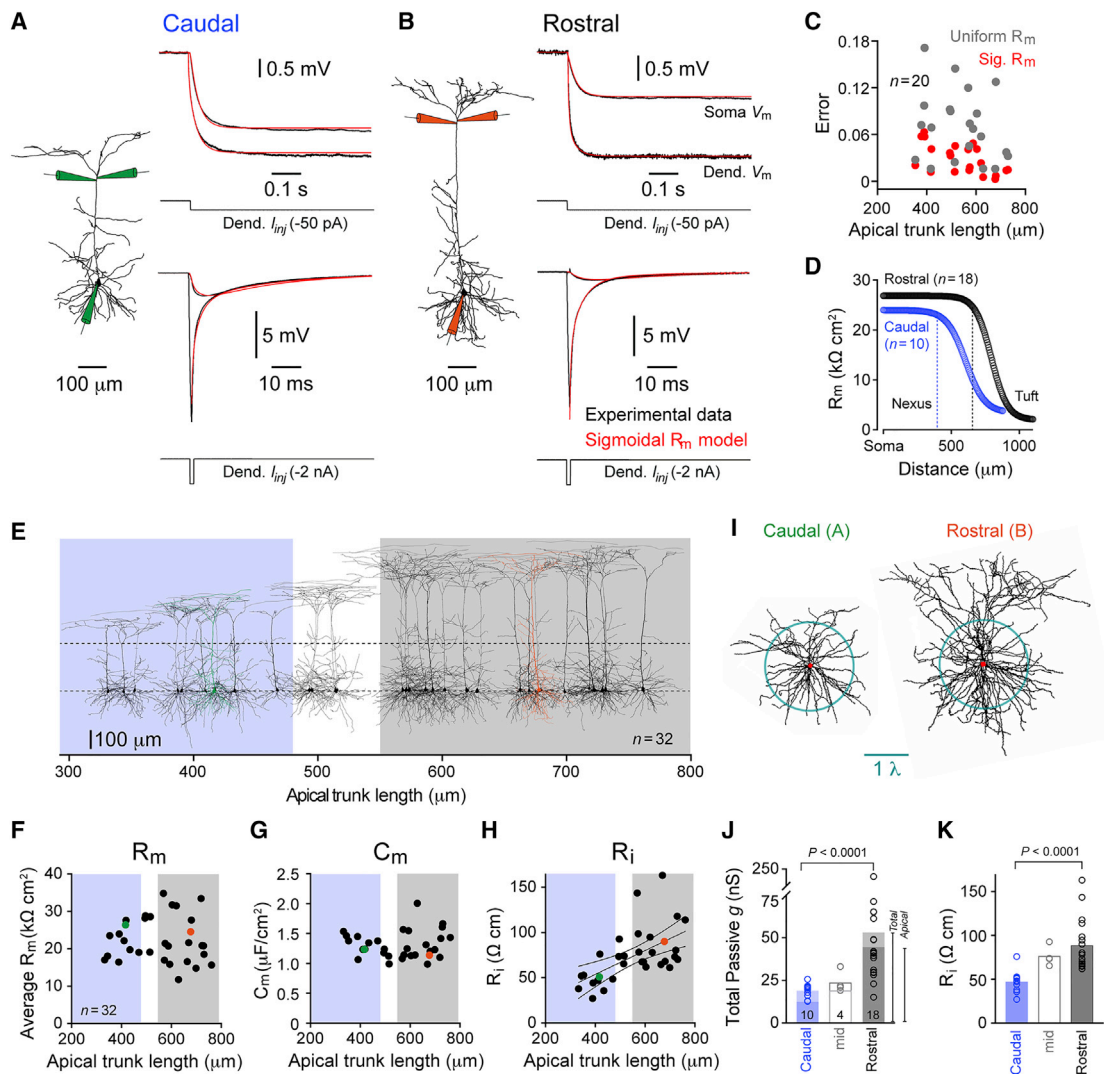


Figure 6. The Intracellular Resistivity of Rostral and Caudal Layer 5B Pyramidal Neurons Is Distinct

(A and B) Passive compartmental models (red traces) with nonuniformly distributed membrane resistance (R_m) accurately simulate experimental voltage (black) traces recorded from the soma and apical dendritic sites of caudal (A) and rostral (B) V1 L5B pyramidal neurons in the presence of ZD7288 (10 μ M) and TTX (1 μ M). The insets show neuronal morphology and the placement of recording electrodes.

(C) Error values obtained by calculation of region fitness between experiment and simulation in uniform R_m (gray symbols) and nonuniform R_m (red symbols) models. The error represents the total error from all traces used for fitting.

(D) Nonuniform distribution of R_m is similar for rostral and caudal L5B pyramidal neurons.

(E) Reconstructions of neurons used for modeling. Blue and gray regions delineate caudal and rostral V1; the neurons colored in green and orange are shown in (A) and (B), respectively.

(F–H) In best-fit models, the average value of R_m (mean of all compartments; F) and specific membrane capacitance (C_m ; G) show no relationship with apical trunk length, whereas specific intracellular resistivity (R_i ; H) demonstrates a correlation with apical trunk length (solid and dotted lines represents the result of linear regression and 95% confidence intervals, respectively).

(I) Dendro-somatic morphoelectrotonic transforms. The radii of the blue circles represent one length constant.

(J) Total mean passive conductance over the entire neuron and apical dendritic arbor; neurons were grouped by apical dendritic trunk length.

(K) Mean R_i of neurons grouped by apical dendritic trunk length.

See also Figures S5 and S6.

ion channel blockers increased apparent input resistance and decreased the dendro-somatic attenuation of voltage in rostral and caudal L5B pyramidal neurons (Figures 7C and 7D; 50% dendro-somatic voltage transfer = 770 μ m). Despite this, under such passive recording conditions, significant difference be-

tween the degree of dendro-somatic voltage attenuation exhibited by rostral and caudal L5B pyramidal neurons were preserved (Figure 7E; caudal [$n = 14$] versus rostral [$n = 11$], t test; control, $p < 0.0001$; ZD7288 + TTX, $p < 0.0001$; cocktail, $p < 0.0001$). Moreover, compartmental modeling and direct

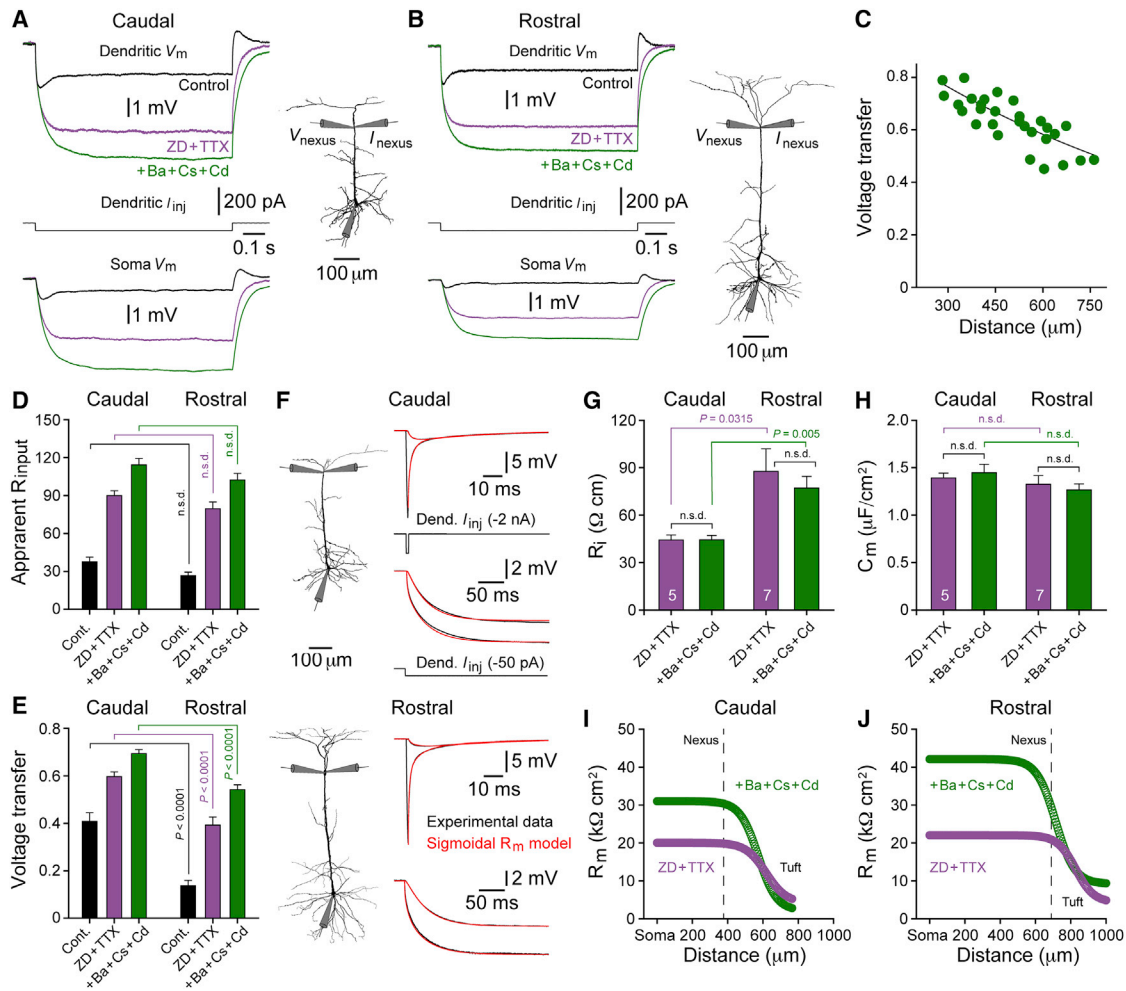


Figure 7. Intracellular Resistivity Determines the Electrical Structure of Rostral and Caudal Layer 5B Pyramidal Neurons

(A and B) Somatic impact of distal apical dendritic voltage responses in a caudal (A) and rostral (B) V1 L5B pyramidal neuron recorded under the indicated conditions (ZD7288, 10 μ M; TTX, 1 μ M; cesium, 3 mM; barium, 0.1 mM; cadmium, 0.1 mM). Voltage responses were evoked in response to negative current steps delivered at dendritic sites. Neuronal morphology and the placement of electrodes are shown.

(C) Dendro-somatic voltage transfer under conditions where resting conductance was pharmacologically blocked (ZD7288, TTX, cesium, barium, and cadmium). The line represents a fit to these data with a single exponential function. All dendritic recordings were made at sites close to the nexus of the apical dendritic trunk (distance from nexus = 30.6 ± 6.1 μ m, $n = 29$).

(D) Pharmacological blockade of resting conductance resulted in an increase in dendritic steady-state apparent input resistance. Apparent input resistance (mean \pm SEM) was similar between caudal and rostral neurons (paired t test; n.s.d., not significantly different).

(E) Pattern of dendro-somatic voltage-attenuation (mean \pm SEM) across the indicated recording conditions for caudal and rostral V1 L5B pyramidal neurons (paired t test).

(F) Passive compartmental models (red traces) with nonuniformly distributed membrane resistance (R_m) accurately simulate experimental voltage (black) traces recorded from the soma and apical dendritic sites of caudal (top) and rostral (bottom) V1 L5B pyramidal neurons in the presence of ZD7288, TTX, cesium, barium, and cadmium. Neuronal morphology and the placement of recording electrodes are shown.

(G) In best-fit models, made under the indicated recording conditions, the average value of R_i (mean \pm SEM) was significantly lower in caudal V1 L5B pyramidal neurons. The R_i of caudal and rostral neurons was unaltered by the addition of cesium, barium, and cadmium to the extracellular solution (unpaired t test).

(H) Values of C_m (mean \pm SEM) remained constant under the indicated recorded conditions (unpaired t test).

(I and J) In best-fit models the addition of cesium, barium, and cadmium increased R_m (mean \pm SEM) but did not alter the nonuniform distribution in caudal (I) or rostral (J) L5B pyramidal neurons.

Bar graphs represent mean \pm SEM.

parameter fitting demonstrated that the best-fit values of R_i and C_m were not altered by the pharmacological antagonism of the remaining classes of voltage-activated channels to preserve the significantly different values of R_i between rostral and caudal

neurons (Figures 7F–7H; R_i all blockers: caudal = 44.4 ± 2.8 Ω cm, $n = 5$; rostral = 77.2 ± 7.4 Ω cm, $n = 7$; t test, $p < 0.005$). Consistent with electrophysiological results, however, the application of this cocktail of ion channel blockers increased the

compartment-dependent value of R_m while preserving the non-uniform R_m distribution across the apical dendritic tree (Figures 7I and 7J). Taken together, therefore, these data illustrate that estimations of the R_i of rostral and caudal L5B pyramidal neurons are distinct when determined under passive recording conditions.

We next examined if our determination of R_i in rostral and caudal V1 L5B pyramidal neurons was model dependent. We first explored if differences in R_i resulted from methods used for the incorporation of dendritic spines. Notably, we found that the best-fit values of R_i were unchanged when the surface area of spinous dendritic compartments were scaled by the commonly used value of two (Stuart and Spruston, 1998), or even when no spine scale was applied, despite the expected shift in R_m and C_m (Figures S7A and S7B). We also examined if differences in R_i were apparent in models that possessed a uniform R_m , finding that distinct R_i values were apparent in simulations where R_m and C_m were constrained to match the experimentally estimated time constant (Stuart and Spruston, 1998) (Figures S6F and S6G; caudal $R_i = 35.7 \pm 4.9 \Omega \text{ cm}$, $n = 6$; rostral $R_i = 59.6 \pm 6.8 \Omega \text{ cm}$, $n = 11$; difference = 23.9 ± 9.96 ; t test, $p = 0.0298$). Notably, uniform R_m models were not as accurate as sigmoidal R_m models at describing membrane charging, but accurately reproduced the steady-state dendro-somatic attenuation of voltage in rostral and caudal L5B pyramidal neurons. We next considered errors associated with the reconstruction of L5B neuron morphology, as the effects of intracellular resistance on charge flow are tightly linked to the diameter of neuronal processes. We reasoned that our methods for the measurement of the diameter of dendritic processes may have been distorted by histological processing and the resolution limits of light microscopy, despite correction for light spread with deconvolution. To explore how such a distortion may influence R_i in model neurons, we scaled the diameter of the morphology of each modeled neuron (Figures S7C–S7G). These procedures revealed that in order to equilibrate R_i between L5B neurons of the rostral and caudal poles of V1, a specific $\sim 20\%$ measurement error of morphological features would have to have occurred solely in either the rostral or caudal groups (Figures S7C–S7E; diameter scale $\times 1.2$). In these models, however, such selective scaling also perturbed other passive parameters, producing values of C_m that were significantly different between rostral ($n = 11$) and caudal ($n = 5$) neurons (Figure S7F; t test, $p = 0.017$). Notably, direct measurement of tissue shrinkage, which was made by comparing dendritic segment length between images obtained live at the electrophysiological setup and following tissue fixation, revealed no difference in the average value between rostral and caudal neurons (Figure S7H; caudal = 0.91 ± 0.02 , $n = 10$; rostral = 0.91 ± 0.02 , $n = 16$). It is therefore unlikely that the observed gradient in R_i is attributable to a systematic error in neurite measurement.

Taken together, therefore, our experimental and simulation results suggest that the passive biophysical properties of V1 L5B pyramidal neurons do not act to normalize the pattern of voltage attenuation imposed by apical dendritic morphology but rather serve to accentuate differences in the electrical structure of rostral and caudal L5B pyramidal neurons. To visualize these differences, we transformed the physical morphology to reflect the

electrotonic size of passive neurons (Zador et al., 1995; Figures 6I and S8). Such morphoelectrotonic transforms depicted the effects of morphological and biophysical differences, demonstrating that the distal dendrites (particularly the apical dendritic tuft) in the rostral neurons were substantially further from the soma in electrotonic distance than in the caudal neurons. Notably, morphoelectrotonic transforms of caudal L5B pyramidal neurons were relatively symmetrical, revealing that voltage attenuation from distal apical tuft dendrites was similar to that from distal basal dendrites, a symmetry not exhibited by rostral L5B pyramidal neurons (Figure 6I). Analysis of morphoelectrotonic transforms allowed us to demonstrate that a combination of morphological and passive biophysical properties underlies the differential dendro-somatic attenuation of voltage in rostral and caudal L5B pyramidal neurons (Figure S8).

Gradient of Associative Integration across V1

In the somatosensory cortex, active dendritic integration in L5B pyramidal neurons has a defining role in neocortical circuit operation, implementing sensori-motor computations through the dynamical interaction of axo-somatic and apical dendritic integration compartments that drive neuronal output correlated with perceptual performance (Takahashi et al., 2016; Xu et al., 2012). As this form of associative integration is reliant on distal apical dendritic electrogenesis, which drives high-frequency AP burst firing (Harnett et al., 2013; Larkum et al., 1999; Williams, 2005; Xu et al., 2012), we explored if the rostro-caudal gradient of the dendritic properties of L5B pyramidal neurons impacted on the representation of this computation in V1. To test this, we generated barrages of simulated EPSPs at somatic and distal apical dendritic sites of rostral and caudal V1 L5B pyramidal neurons (Figures 8A and 8B). When an excitatory input was delivered to the soma alone, a low-frequency pattern of AP firing was generated (Figures 8A and 8B; AP frequency: caudal = $9.4 \pm 0.2 \text{ Hz}$, $n = 203$ trials, $n = 14$ neurons; rostral = $8.9 \pm 0.1 \text{ Hz}$; $n = 321$ trials, $n = 21$ neurons). In contrast, when excitatory input was concomitantly delivered to the soma and distal apical dendritic sites, we observed divergent patterns of associative integration between rostral and caudal L5B pyramidal neurons (Figures 8A and 8B; dendritic recordings made $33.2 \pm 4.6 \mu\text{m}$ from the nexus, $n = 41$). This bifurcation of associative integration was found to be independent of the precise composition of dendritic excitatory input and was manifest when dendritic excitation was composed of EPSPs injected as ideal current sources or as dual-component AMPA:NMDA EPSPs using dynamic-clamp techniques. In rostral L5B pyramidal neurons, associative integration elevated AP firing rates, leading to the generation of high-frequency AP burst firing, initiated by dendritic spikes, to render the AP output highly variable (Figures 8A, 8C, and 8E; ideal current dendritic EPSPs: CV across dendritic input range = 1.08 ± 0.02 ; APs generated at instantaneous frequencies $>100 \text{ Hz} = 28.9\%$; dendritic dynamic-clamp EPSPs: CV across dendritic input range = 1.21 ± 0.03 ; APs generated at instantaneous frequencies $>100 \text{ Hz} = 25.6\%$). Analysis revealed that associative integration in rostral neurons led to AP output that deviated from the simple linear summation of AP firing generated by somatic or dendritic input alone as the dendritic input rate increased, subsequently plateaued at supra-linear

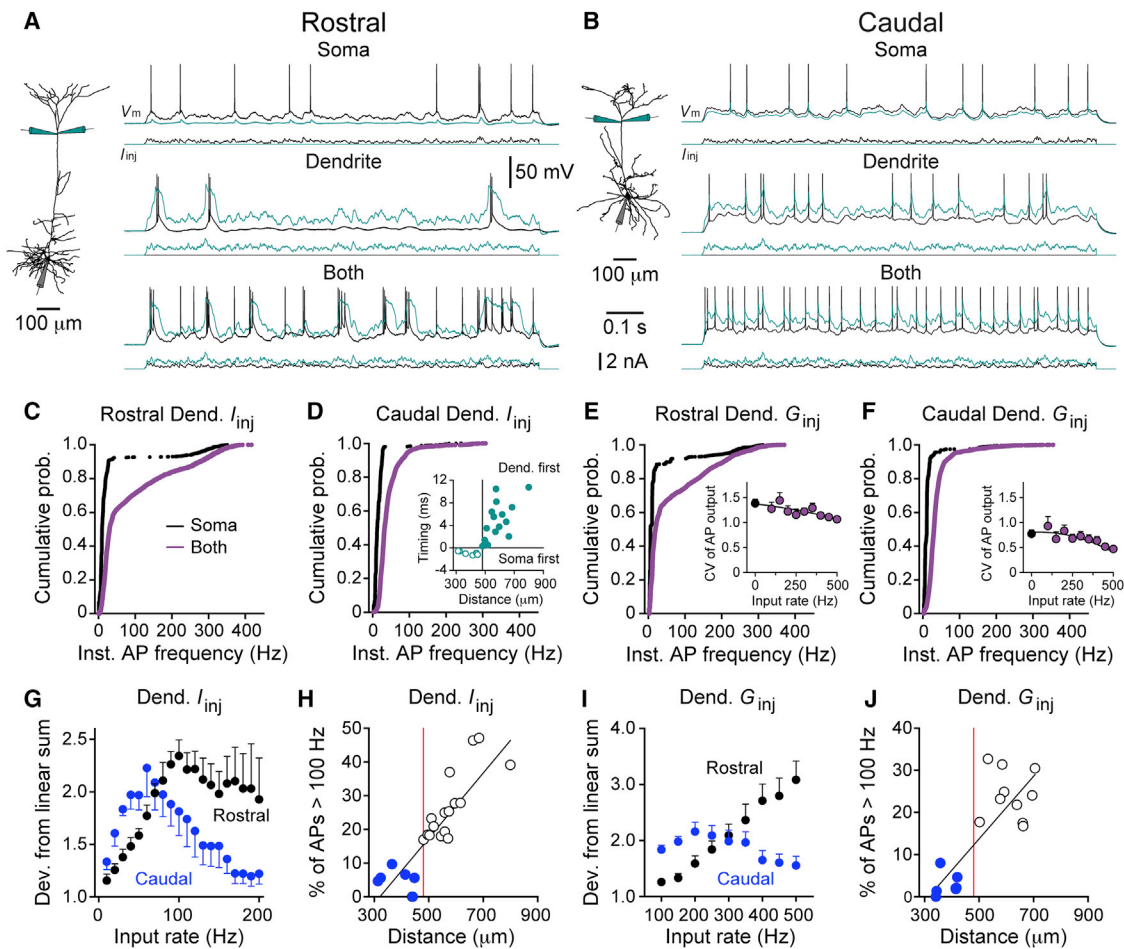


Figure 8. Representation of a Neuronal Computation across the Rostro-caudal Axis of V1

(A and B) Distinct patterns of associative integration of somatic (black) and dendritic (green) input by rostral (A) and caudal (B) L5B pyramidal neurons. Simultaneously recorded somatic (black, V_m) and distal apical dendritic (green, V_m) voltage responses generated by barrages of excitatory postsynaptic current (EPSC)-shaped ideal current waveforms (I_{inj}) delivered at somatic or distal apical dendritic sites and following the pairing of these inputs (both). Morphology of recorded neurons and electrode placement are shown in the insets.

(C and D) Cumulative probability plots of the instantaneous frequency of AP firing in response to somatic (black) or combined somatic and dendritic (purple) ideal current input for rostral (C; $n = 12$) and caudal L5B pyramidal neurons (D; $n = 7$). The inset graph shows the latency difference between regenerative spikes recorded at somatic and dendritic sites in response to dendritic excitatory input as a function of apical dendritic trunk length. The vertical line demarks the trunk length at which dendritic spikes first preceded AP output (Dend. first), which is also indicated by the red lines in (H) and (J).

(E and F) Cumulative probability plots of the instantaneous frequency of AP firing in response to somatic barrages (black symbols) and paired presentation of AMPA:NMDA conductance (G_{inj} ; purple symbols) injected at distal apical dendritic sites in rostral (E; $n = 8$) and caudal L5B pyramidal neurons (F; $n = 7$). The inset graphs illustrate the coefficient of variation of AP firing across the frequency range of dendritic excitatory conductance (mean \pm SEM).

(G and I) The AP output generated during associative integration was greater than the linear sum of AP output evoked by somatic and dendritic input alone when dendritic input was injected as an ideal current (G) or excitatory conductance (I) (mean \pm SEM).

(H and J) Relationship between apical dendritic recording site and the fraction of APs generated at instantaneous frequencies >100 Hz during the associative integration of distal apical dendritic and somatic excitatory input when dendritic input was injected as an ideal current (H) or excitatory conductance (J). The lines represent the results of linear regression.

values as the input frequency of ideal current injected dendritic EPSPs was further increased (Figure 8G), or continued to rise when dendritic input was driven by simulated dual-component AMPA:NMDA EPSPs, presumably because of the sustained dendritic depolarization produced by the simulated NMDA conductance (Figure 8I). In contrast, in caudal neurons, associative integration powerfully drove AP output but did not lead to a highly variable AP firing pattern or the generation of AP burst

firing (Figures 8B, 8D, and 8F; ideal current dendritic EPSPs: CV across dendritic input range = 0.69 ± 0.03 ; APs generated at instantaneous frequencies >100 Hz = 4.9%; dendritic dynamic-clamp EPSPs: CV across dendritic input range = 0.68 ± 0.04 ; APs generated at instantaneous frequencies >100 Hz = 4.4%). Associative integration in caudal neurons led to AP output that sharply deviated from the simple linear summation of AP firing generated by somatic or dendritic input alone, but then

declined to near linear summation as the frequency of generation of dendritic EPSPs was further increased (Figures 8G and 8I). Notably, in neurons recorded across V1, we observed a linear relationship between dendritic trunk length and the fraction of APs generated at high frequencies during associative integration (Figures 8H and 8J; ideal current dendritic EPSPs: linear regression slope = $9.7 \pm 1.3\%$ per 100 μm , $r^2 = 0.71$, $F = 53.2$, $p < 0.0001$; dendritic dynamic-clamp EPSPs: linear regression slope = $7.4 \pm 1.4\%$ per 100 μm , $r^2 = 0.66$, $F = 29.16$, $p < 0.0001$). Thus, proximal and distal dendritic streams of excitatory input are associatively integrated in rostral and caudal V1 L5B pyramidal neurons by different mechanisms to form distinct patterns of neuronal output. We suggest that the simple associative computation executed by caudal V1 L5B pyramidal neurons is mediated by the direct impact of dendritic excitatory input on axo-somatic integration. Consistent with this idea, we qualitatively reproduced this computation in model caudal L5B pyramidal neurons, which expressed active conductances exclusively in somatic compartments (Figure S9). In contrast, such simple models failed to reproduce the computational operations of rostral L5B pyramidal neurons, as models lacked active dendritic integration (Figure S9). Taken together, these data reveal a gradient of the representation of a fundamental neuronal computation across the rat primary visual cortex.

DISCUSSION

High-resolution structural MRI demonstrated that neocortical thickness exhibits a declining rostral-to-caudal gradient across the primary visual cortex of the rat. This gradient controlled the length, but not the diameter, of the apical dendrites of L5B pyramidal neurons to govern the anatomical separation between apical tuft and peri-somatic regions of these neurons. Previous functional studies have shown that the emergent computational properties of L5B pyramidal neurons are reliant on the electrical separation between apical dendritic and somatic sites (Harnett et al., 2013; Larkum, 2013; Larkum et al., 1999; Stuart and Spruston, 2015; Williams and Stuart, 2002; Xu et al., 2012). If, as commonly argued, the neocortex is arranged in canonical networks composed of neuronal classes that perform stereotyped computations (Douglas and Martin, 2004; Harris and Shepherd, 2015; Markram et al., 2015), then the electrical properties of a given neuronal class should be conserved across the neocortex to preserve function, despite divergent dendritic morphology (Wittenberg and Wang, 2007). In stark contrast to this expectation, we find that L5B pyramidal neurons recorded across the rostro-caudal gradient of V1 displayed distinct electrical and computational properties. Rostral V1 L5B pyramidal neurons exhibited multisite active dendritic integration and were highly electrically compartmentalized. In contrast, caudal L5B pyramidal neurons were electrically compact, and dendritic excitatory input was not locally integrated in the dendritic arbor. Caudal neurons therefore function as relatively compact axo-somatic integrators, where dendritic excitatory input spreads directly to the soma and axon to influence AP output in a manner analogous to L2/3 pyramidal neurons of the somatosensory neocortex (Palmer et al., 2014). Thus, changes in the length of the apical dendritic arbor of L5B pyramidal neurons imposed by the anat-

omy of the brain and skull are neither compensated for electrically by the alteration of biophysical properties nor morphologically by the adjustment of dendritic diameter. This gradient in morphology, however, resulted in a divergence in the somato-dendritic input to AP output transformations executed by L5B pyramidal neurons to produce quantitatively different AP firing patterns, characterized by the selective generation of high-frequency AP burst firing in rostral L5B pyramidal neurons, which has significant implications for downstream signaling (Williams, 2005).

Remarkably, we observed a key determinant of neuronal electrical architecture, intracellular resistivity, was significantly lower in caudal L5B pyramidal neurons and increased in a gradient as recordings were made from L5B neurons positioned rostrally in V1. Our simulations replicated all other key facets of the passive properties of L5B pyramidal neurons, including the decline in specific membrane resistance at distal apical dendritic sites (Stuart and Spruston, 1998). Indeed, simulation of rostral V1 L5B pyramidal neurons revealed biophysical parameters closely matched to those estimated from L5B pyramidal neurons of the somatosensory neocortex (Stuart and Spruston, 1998). Despite our use of simultaneous somatic and dual-dendritic recording techniques to obviate dendritic bridge balance artifacts (Williams and Stuart, 2002), caveats in the determination of the electrotonic architecture of neurons using direct parameter fitting to experimental data remain, such as the assumption of extracellular isopotentiality, the lack of ionic depletion or accumulation, uniformity of charge across the core conductor, and the non-uniqueness issue created by the spatially distributed, nonuniform structure and membrane resistance of pyramidal neurons (Major et al., 1994; Stuart and Spruston, 1998). The close similarity between the biophysical parameters estimated from large L5B pyramidal neurons of rostral V1 to those of the somatosensory neocortex (Stuart and Spruston, 1998) suggests that the gradient of R_i that we describe for L5B neurons across the rostro-caudal axis of V1 is noteworthy. How then could R_i vary between neurons that share a similar general structure and genetic (Kim et al., 2015) and developmental (Maruoka et al., 2017) origin?

Intracellular resistivity is thought to be primarily influenced by the molecule concentrations within the cytosol, the presence and distribution of intracellular organelles, and the composition of the cytoskeleton. Considering the use of identical triple whole-cell recording techniques and identical extra- and intracellular solutions between recordings, it is unlikely that the cytosolic ionic and organic molecule concentrations differed between rostral and caudal neurons. It is, however, known that dendritic organelles (primarily the endoplasmic reticulum [ER] and mitochondria) can be highly dynamic, particularly during neuronal circuit development (Faits et al., 2016; Fukumitsu et al., 2015); for example, mitochondria localize and aggregate at sites of high activity and calcium influx (Barnhart, 2016; Fukumitsu et al., 2015), and dendritic mitochondria are structurally dynamic during calcium-dependent synaptic plasticity (Divakaruni et al., 2018). Both mitochondria and the ER form extensive, elongated networks within dendrites, occupying a significant though variable proportion of the cytosolic volume (Kasthuri et al., 2015; Popov et al., 2005). It is conceivable the enrichment and/or structural alteration of the ER and mitochondria is

required to support the additional energy expenditure (Haller-mann et al., 2012), calcium regulation (Rizzuto et al., 2012), and protein biosynthesis (Rangaraju et al., 2017) that underlie active dendritic integration in L5B pyramidal neurons of rostral V1. For example, the generation of large calcium-mediated dendritic plateau potentials (Larkum et al., 2009) would lead to additional ATP and biosynthesis requirements for establishing and resetting cytosolic and internal store calcium concentration (Hof-warth et al., 2012). Additional organelles at apical dendritic sites to support these functions with no compensatory change in dendritic diameter (as observed here) would therefore be predicted to influence R_i . Thus, we suggest a fundamental building block of the electrical architecture of neurons, R_i , is not uniform in a given neuronal class but determined by the molecular mechanisms responsible for emergent computational operations, perhaps shaped in response to the developmental refinement of neuronal circuit activity (Faits et al., 2016; Fukumitsu et al., 2015; Maruoka et al., 2017). The confirmation of this idea, however, requires future investigation of the structural elements that define R_i , such as the distribution of subcellular organelles in identified L5B neurons of rostral and caudal V1.

Functionally, intracellular resistance is one of the factors that influence charge transfer from dendritic sites to the soma and axon. In rostral V1 L5B pyramidal neurons, the relatively higher value of R_i will limit dendro-somatic charge transfer and so acts to enhance the ability of distal apical dendritic excitatory input to depolarize the dendritic membrane to reach the threshold for dendritic spike initiation. In contrast, the lower R_i in caudal V1 L5B pyramidal neurons will promote dendro-somatic charge transfer, allowing distal dendritic excitatory input to have a proportionally greater direct impact at the axonal site of AP initiation, mitigating the necessity for local dendritic integration and amplification. Thus, rather than compensating for neocortical-thickness-imposed shortening of the apical dendritic arbor, the lower R_i of caudal L5B pyramidal neurons accentuates electrical compactness. Notably, rats exhibit extremely sensitive defensive behaviors in response to moving stimuli that mimic overhead, avian predators (Wallace et al., 2013), a region of visual space analyzed by the caudal pole of V1 (Gias et al., 2005). Our findings suggest that excitatory synaptic input to the apical tuft of caudal L5B pyramidal neurons, which include motion-related visual signals (Cruz-Martín et al., 2014), will have a direct influence on neuronal output, but this sensitivity to dendritic synaptic input comes at a cost, limiting the range and robustness of the computational operations executed by caudal L5B pyramidal neurons.

In the working brain, a high synaptic conductance state has been shown to impact the electrophysiological properties of neurons (Destexhe et al., 2003), acting as a balanced and distributed conductance that limits dendro-somatic voltage transfer (Bernander et al., 1991; Williams, 2004). Although a high-conductance state accentuates dendro-somatic voltage attenuation in the subthreshold domain, it does not influence the forward propagation of dendritic spikes or their coupling to AP output in L5B pyramidal neurons of the somatosensory cortex (Williams, 2004, 2005). Thus, the impact of dendritic excitatory input on AP output would be predicted to be distinct in caudal and rostral V1 L5B pyramidal neurons as network activity

levels vary because of contrasting integrative mechanisms, with increased activity limiting the impact of dendritic excitatory input on AP output in caudal V1 L5B pyramidal neurons. In contrast, active compartmentalized apical dendritic and associative integration in rostral V1 L5B pyramidal neurons will remain robust to changes in conductance state (Williams, 2004, 2005). Interestingly, algorithms inspired by the active dendritic integrative mechanisms of L5B pyramidal neurons can exhibit deep learning without the need for the biologically implausible back-propagation of error; however, electrotonic separation between segregated compartments is essential (Guerquiev et al., 2017), underscoring the importance of our findings of distinct associative computations executed by rostral and caudal V1 L5B pyramidal neurons. It is tempting to extrapolate this finding to other neocortical areas and species, as neocortical thickness of humans and other primates is enlarged in areas that underlie complex associative integration tasks (Cahalane et al., 2012; Thiebaut de Schotten et al., 2017; Wagstyl et al., 2015).

In summary, our findings contribute to the growing body of evidence highlighting the functional heterogeneity of neuronal classes in cortical networks, which parallel electrophysiological, morphological, and molecular gradients (Cembrowski et al., 2016; Garden et al., 2008; Malik and Johnston, 2017; Strange et al., 2014). Functionally, our work suggests that gradients in the gross neuroanatomy of the neocortex, single-cell morphology, and biophysics act to impose flexibility in the computational strategies employed in neocortical microcircuits.

STAR★METHODS

Detailed methods are provided in the online version of this paper and include the following:

- KEY RESOURCES TABLE
- CONTACT FOR REAGENT AND RESOURCE SHARING
- EXPERIMENTAL MODEL AND SUBJECT DETAILS
 - Animals
- METHOD DETAILS
 - Structural Magnetic Resonance Imaging
 - Brain slice preparation
 - Whole-cell recordings
 - Microscopy and neuronal reconstruction
 - Retrograde labeling
 - Computational modeling and parameter fitting
 - Experimental design
- QUANTIFICATION AND STATISTICAL ANALYSIS
 - Morphological quantification
 - Statistical quantification and analysis
- DATA AND SOFTWARE AVAILABILITY

SUPPLEMENTAL INFORMATION

Supplemental Information includes nine figures and can be found with this article online at <https://doi.org/10.1016/j.neuron.2018.10.048>.

ACKNOWLEDGMENTS

The authors thank Drs. N. Kurniawan, A. Janke, and F. Cotel for advice and assistance with MRI and stereotaxic injections. L.N.F. was supported by an

Australian Government Postgraduate Award (42836900). S.R.W. was supported by the Hand Heart Pocket Foundation (RM2012002179), the National Health and Medical Research Council (grant GNT1082257), and the Australian Research Council (grant DP130101630).

AUTHOR CONTRIBUTIONS

L.N.F. and S.R.W. performed and designed research, analyzed data, and wrote the paper.

DECLARATION OF INTERESTS

The authors declare no competing interests.

Received: December 12, 2017

Revised: August 3, 2018

Accepted: October 25, 2018

Published: November 21, 2018

REFERENCES

- Barnhart, E.L. (2016). Mechanics of mitochondrial motility in neurons. *Curr. Opin. Cell Biol.* 38, 90–99.
- Bernander, O., Douglas, R.J., Martin, K.A., and Koch, C. (1991). Synaptic background activity influences spatiotemporal integration in single pyramidal cells. *Proc. Natl. Acad. Sci. USA* 88, 11569–11573.
- Bittner, K.C., Grienberger, C., Vaidya, S.P., Milstein, A.D., Macklin, J.J., Suh, J., Tonegawa, S., and Magee, J.C. (2015). Conjunctive input processing drives feature selectivity in hippocampal CA1 neurons. *Nat. Neurosci.* 18, 1133–1142.
- Branco, T., and Häusser, M. (2010). The single dendritic branch as a fundamental functional unit in the nervous system. *Curr. Opin. Neurobiol.* 20, 494–502.
- Cahalane, D.J., Charvet, C.J., and Finlay, B.L. (2012). Systematic, balancing gradients in neuron density and number across the primate isocortex. *Front. Neuroanat.* 6, 28.
- Cembrowski, M.S., Bachman, J.L., Wang, L., Sugino, K., Shields, B.C., and Spruston, N. (2016). Spatial gene-expression gradients underlie prominent heterogeneity of CA1 pyramidal neurons. *Neuron* 89, 351–368.
- Cruz-Martín, A., El-Danaf, R.N., Osakada, F., Sriram, B., Dhande, O.S., Nguyen, P.L., Callaway, E.M., Ghosh, A., and Huberman, A.D. (2014). A dedicated circuit links direction-selective retinal ganglion cells to the primary visual cortex. *Nature* 507, 358–361.
- Destexhe, A., Rudolph, M., and Paré, D. (2003). The high-conductance state of neocortical neurons in vivo. *Nat. Rev. Neurosci.* 4, 739–751.
- Divakaruni, S.S., Van Dyke, A.M., Chandra, R., LeGates, T.A., Contreras, M., Dharmasri, P.A., Higgs, H.N., Lobo, M.K., Thompson, S.M., and Blanpied, T.A. (2018). Long-Term Potentiation Requires a Rapid Burst of Dendritic Mitochondrial Fission during Induction. *Neuron* 100, 1–16.
- Douglas, R.J., and Martin, K.A.C. (2004). Neuronal circuits of the neocortex. *Annu. Rev. Neurosci.* 27, 419–451.
- Faits, M.C., Zhang, C., Soto, F., and Kerschensteiner, D. (2016). Dendritic mitochondria reach stable positions during circuit development. *eLife* 5, e11583.
- Fukumitsu, K., Fujishima, K., Yoshimura, A., Wu, Y.K., Heuser, J., and Kengaku, M. (2015). Synergistic action of dendritic mitochondria and creatine kinase maintains ATP homeostasis and actin dynamics in growing neuronal dendrites. *J. Neurosci.* 35, 5707–5723.
- Garden, D.L.F., Dodson, P.D., O'Donnell, C., White, M.D., and Nolan, M.F. (2008). Tuning of synaptic integration in the medial entorhinal cortex to the organization of grid cell firing fields. *Neuron* 60, 875–889.
- Gias, C., Hewson-Stoate, N., Jones, M., Johnston, D., Mayhew, J.E., and Coffey, P.J. (2005). Retinotopy within rat primary visual cortex using optical imaging. *Neuroimage* 24, 200–206.
- Glasser, M.F., Coalson, T.S., Robinson, E.C., Hacker, C.D., Harwell, J., Yacoub, E., Ugurbil, K., Andersson, J., Beckmann, C.F., Jenkinson, M., et al. (2016). A multi-modal parcellation of human cerebral cortex. *Nature* 536, 171–178.
- Guerguiev, J., Lillicrap, T.P., and Richards, B.A. (2017). Towards deep learning with segregated dendrites. *eLife* 6, e22901.
- Hallermann, S., de Kock, C.P.J., Stuart, G.J., and Kole, M.H.P. (2012). State and location dependence of action potential metabolic cost in cortical pyramidal neurons. *Nat. Neurosci.* 15, 1007–1014.
- Harnett, M.T., Xu, N.-L., Magee, J.C., and Williams, S.R. (2013). Potassium channels control the interaction between active dendritic integration compartments in layer 5 cortical pyramidal neurons. *Neuron* 79, 516–529.
- Harnett, M.T., Magee, J.C., and Williams, S.R. (2015). Distribution and function of HCN channels in the apical dendritic tuft of neocortical pyramidal neurons. *J. Neurosci.* 35, 1024–1037.
- Harris, K.D., and Shepherd, G.M.G. (2015). The neocortical circuit: themes and variations. *Nat. Neurosci.* 18, 170–181.
- Hines, M.L., and Carnevale, N.T. (1997). The NEURON simulation environment. *Neural Comput.* 9, 1179–1209.
- Howarth, C., Gleeson, P., and Attwell, D. (2012). Updated energy budgets for neural computation in the neocortex and cerebellum. *J. Cereb. Blood Flow Metab.* 32, 1222–1232.
- Janke, A.L., and Ullmann, J.F.P. (2015). Robust methods to create ex vivo minimum deformation atlases for brain mapping. *Methods* 73, 18–26.
- Kasthuri, N., Hayworth, K.J., Berger, D.R., Schalek, R.L., Conchello, J.A., Knowles-Barley, S., Lee, D., Vázquez-Reina, A., Kaynig, V., Jones, T.R., et al. (2015). Saturated reconstruction of a volume of neocortex. *Cell* 162, 648–661.
- Kim, E.J., Juavinett, A.L., Kyubwa, E.M., Jacobs, M.W., and Callaway, E.M. (2015). Three types of cortical layer 5 neurons that differ in brain-wide connectivity and function. *Neuron* 88, 1253–1267.
- Larkman, A.U. (1991). Dendritic morphology of pyramidal neurones of the visual cortex of the rat: III. Spine distributions. *J. Comp. Neurol.* 306, 332–343.
- Larkum, M. (2013). A cellular mechanism for cortical associations: an organizing principle for the cerebral cortex. *Trends Neurosci.* 36, 141–151.
- Larkum, M.E., Zhu, J.J., and Sakmann, B. (1999). A new cellular mechanism for coupling inputs arriving at different cortical layers. *Nature* 398, 338–341.
- Larkum, M.E., Nevian, T., Sandler, M., Polsky, A., and Schiller, J. (2009). Synaptic integration in tuft dendrites of layer 5 pyramidal neurons: a new unifying principle. *Science* 325, 756–760.
- Losonczy, A., Makara, J.K., and Magee, J.C. (2008). Compartmentalized dendritic plasticity and input feature storage in neurons. *Nature* 452, 436–441.
- Major, G., Larkman, A.U., Jonas, P., Sakmann, B., and Jack, J.J. (1994). Detailed passive cable models of whole-cell recorded CA3 pyramidal neurons in rat hippocampal slices. *J. Neurosci.* 14, 4613–4638.
- Malik, R., and Johnston, D. (2017). Dendritic GIRK channels gate the integration window, plateau potentials, and induction of synaptic plasticity in dorsal but not ventral CA1 neurons. *J. Neurosci.* 37, 3940–3955.
- Markram, H., Müller, E., Ramaswamy, S., Reimann, M.W., Abdellah, M., Sanchez, C.A., Ailamaki, A., Alonso-Nanclares, L., Antille, N., Arsever, S., et al. (2015). Reconstruction and simulation of neocortical microcircuitry. *Cell* 163, 456–492.
- Maruoka, H., Nakagawa, N., Tsuruno, S., Sakai, S., Yoneda, T., and Hosoya, T. (2017). Lattice system of functionally distinct cell types in the neocortex. *Science* 358, 610–615.
- Müller, C., Beck, H., Coulter, D., and Remy, S. (2012). Inhibitory control of linear and supralinear dendritic excitation in CA1 pyramidal neurons. *Neuron* 75, 851–864.
- Palmer, L.M., Shai, A.S., Reeve, J.E., Anderson, H.L., Paulsen, O., and Larkum, M.E. (2014). NMDA spikes enhance action potential generation during sensory input. *Nat. Neurosci.* 17, 383–390.

- Paxinos, G., and Watson, C. (2007). *The Rat Brain in Stereotaxic Coordinates*, Sixth Edition (Elsevier).
- Poirazi, P., Brannon, T., and Mel, B.W. (2003). Pyramidal neuron as two-layer neural network. *Neuron* 37, 989–999.
- Polsky, A., Mel, B.W., and Schiller, J. (2004). Computational subunits in thin dendrites of pyramidal cells. *Nat. Neurosci.* 7, 621–627.
- Popov, V., Medvedev, N.I., Davies, H.A., and Stewart, M.G. (2005). Mitochondria form a filamentous reticular network in hippocampal dendrites but are present as discrete bodies in axons: a three-dimensional ultrastructural study. *J. Comp. Neurol.* 492, 50–65.
- Rangaraju, V., Tom Dieck, S., and Schuman, E.M. (2017). Local translation in neuronal compartments: how local is local? *EMBO Rep.* 18, 693–711.
- Rizzuto, R., De Stefani, D., Raffaello, A., and Mammucari, C. (2012). Mitochondria as sensors and regulators of calcium signalling. *Nat. Rev. Mol. Cell Biol.* 13, 566–578.
- Rockel, A.J., Hiorns, R.W., and Powell, T.P.S. (1980). The basic uniformity in structure of the neocortex. *Brain* 103, 221–244.
- Schiller, J., Major, G., Koester, H.J., and Schiller, Y. (2000). NMDA spikes in basal dendrites of cortical pyramidal neurons. *Nature* 404, 285–289.
- Sivyer, B., and Williams, S.R. (2013). Direction selectivity is computed by active dendritic integration in retinal ganglion cells. *Nat. Neurosci.* 16, 1848–1856.
- Smith, S.L., Smith, I.T., Branco, T., and Häusser, M. (2013). Dendritic spikes enhance stimulus selectivity in cortical neurons in vivo. *Nature* 503, 115–120.
- Strange, B.A., Witter, M.P., Lein, E.S., and Moser, E.I. (2014). Functional organization of the hippocampal longitudinal axis. *Nat. Rev. Neurosci.* 15, 655–669.
- Stuart, G. (1999). Voltage-activated sodium channels amplify inhibition in neocortical pyramidal neurons. *Nat. Neurosci.* 2, 144–150.
- Stuart, G., and Spruston, N. (1998). Determinants of voltage attenuation in neocortical pyramidal neuron dendrites. *J. Neurosci.* 18, 3501–3510.
- Stuart, G.J., and Spruston, N. (2015). Dendritic integration: 60 years of progress. *Nat. Neurosci.* 18, 1713–1721.
- Takahashi, N., Oertner, T.G., Hegemann, P., and Larkum, M.E. (2016). Active cortical dendrites modulate perception. *Science* 354, 1587–1590.
- Thiebaut de Schotten, M., Urbanski, M., Batrancourt, B., Levy, R., Dubois, B., Cerliani, L., and Volle, E. (2017). Rostro-caudal architecture of the frontal lobes in humans. *Cereb. Cortex* 27, 4033–4047.
- van Hemmen, J.L., and Sejnowski, T.J. (2006). *23 Problems in Systems Neuroscience*, First Edition (Oxford University Press).
- Vetter, P., Roth, A., and Häusser, M. (2001). Propagation of action potentials in dendrites depends on dendritic morphology. *J. Neurophysiol.* 85, 926–937.
- Wagstyl, K., Ronan, L., Goodyer, I.M., and Fletcher, P.C. (2015). Cortical thickness gradients in structural hierarchies. *Neuroimage* 111, 241–250.
- Wallace, D.J., Greenberg, D.S., Sawinski, J., Rulla, S., Notaro, G., and Kerr, J.N.D. (2013). Rats maintain an overhead binocular field at the expense of constant fusion. *Nature* 498, 65–69.
- Williams, S.R. (2004). Spatial compartmentalization and functional impact of conductance in pyramidal neurons. *Nat. Neurosci.* 7, 961–967.
- Williams, S.R. (2005). Encoding and decoding of dendritic excitation during active states in pyramidal neurons. *J. Neurosci.* 25, 5894–5902.
- Williams, S.R., and Stuart, G.J. (2002). Dependence of EPSP efficacy on synapse location in neocortical pyramidal neurons. *Science* 295, 1907–1910.
- Wittenberg, G.M., and Wang, S.S.H. (2007). Evolution and scaling of dendrites. In *Dendrites*, G. Stuart, N. Spruston, and M. Häusser, eds. (Oxford University Press), pp. 43–67.
- Xu, N.-L., Harnett, M.T., Williams, S.R., Huber, D., O'Connor, D.H., Svoboda, K., and Magee, J.C. (2012). Nonlinear dendritic integration of sensory and motor input during an active sensing task. *Nature* 492, 247–251.
- Zador, A.M., Agmon-Snir, H., and Segev, I. (1995). The morphoelectrotonic transform: a graphical approach to dendritic function. *J. Neurosci.* 15, 1669–1682.

STAR★METHODS

KEY RESOURCES TABLE

REAGENT or RESOURCE	SOURCE	IDENTIFIER
Antibodies		
Rabbit polyclonal vGLUT-2	Synaptic systems	Cat:135403; Lot#: 135403/33 RRID:AB_887883
Chemicals, Peptides, and Recombinant Proteins		
Ionic gadopentetate dimeglumine (Gd-DTPA); Magnevist	Berlex	N/A
CNQX	Tocris	CAS: 115066-14-3
DL-AP5	Tocris	CAS: 79055-68-8
SR 95531	Tocris	CAS: 104104-50-9
CGP52432	Tocris	CAS: 139667-74-6
ZD7288	Tocris	CAS: 133059-99-1
TTX	Alomone	CAS: 18660-81-6
Biocytin	Sigma	CAS: 576-19-2
Streptavidin-Alexa	Invitrogen	Cat#: S11223
Red RetroBeads IX	Lumafluor	N/A
Experimental Models: Organisms/Strains		
Wistar rats	ARC Wistar colony	RGD Cat# 13508588; RRID:RGD_13508588
Software and Algorithms		
computeSurfDist		https://github.com/richardbeare/simplemeshtools
ParaView (v5.4.0)	Paraview	https://www.paraview.org/
3D Slicer (v4.6.2)		https://www.slicer.org/
ITK-SNAP 3.6.0		http://www.itksnap.org/pmwiki/pmwiki.php
Axograph X (1.6.4)	Axograph	N/A
Prism (7)	Graphpad	N/A
SigmaPlot (13)	SysStat Software	N/A
Microsoft Excel (16.5)	Microsoft	N/A
Slidebook (6.0)	3i Intelligent Imaging Innovations	N/A
Huygens Professional (v17.04)	Scientific Volume Imaging	N/A
NeuroLucida	MicroBrightField	N/A
NeuroLucida Explorer	MicroBrightField	N/A
NEURON simulation environment v7.3	Hines and Carnevale, 1997	https://www.neuron.yale.edu/neuron/

CONTACT FOR REAGENT AND RESOURCE SHARING

Further information and requests for resources and reagents should be directed to and will be fulfilled by the Lead Contact, Stephen Williams (srw@uq.edu.au).

EXPERIMENTAL MODEL AND SUBJECT DETAILS

Animals

All experiments were approved by the Animal Ethics Committee of The University of Queensland in accordance with the Australian Code of Practice for the care and use of animals for scientific purposes.

Animals (Wistar rats, RGD Cat# 13508588, RRID:RGD_13508588) were obtained from the Australian Research Council, Western Australian Wistar rat colony. Structural magnetic resonance imaging experiments were performed using Wistar rats (n = 5, male, P35 - P40). Electrophysiological experiments were conducted on brain slices of Wistar rats (male, P26 - P36).

METHOD DETAILS

Structural Magnetic Resonance Imaging

Rats were deeply anesthetized and slowly transcardially perfused (6.4 mL/min) with phosphate buffered saline (PBS, 100 ml), followed by fresh, filtered ultra-pure paraformaldehyde (PFA, 4%, 400 ml, Sigma). The animal was decapitated and the head stored in 4% PFA for 24 hours. The head was subsequently washed with PBS and the brain-case dissected. Holes were drilled in the skull with a dental drill, followed by incubation in ionic gadopentetate dimeglumine (Gd-DTPA, Magnevist, Berlex) for one week. A 3D T1-weighted gradient echo sequence of the encased brains was obtained using a 16.4 T small animal MRI scanner at 50 μ m isotropic resolution.

Images were pre-processed, registered and averaged. A detailed description of the performance of these techniques is provided in (Janke and Ullmann, 2015). To calculate neocortical thickness, the neocortical surface and the corpus callosum were segmented and the perpendicular distance between these structures determined. The brain's surface and the corpus callosum of the resulting registered average were segmented using semi-automatic active contour segmentation, and subsequently refined at every slice in all three axes (ITK-SNAP 3.6.0). The perpendicular distance between the nearest points between the cortical surface and the outer surface of the corpus callosum were calculated using an algorithm developed by Richard Beare (computeSurfDist, <https://github.com/richardbeare/simplemeshtools>). Models were visualized with ParaView (v5.4.0) and 3D Slicer (v4.6.2). Note that the exact measurements at the prefrontal pole of the cortex were subject to error due to the lack of detectable white matter defining the lower boundary of the cortex. The borders of V1, including both the monocular and binocular regions, were delineated by comparison of histological coronal sections of the rat brain (Paxinos and Watson, 2007) with MRI coronal sections. Manual measurement of neocortical thickness was performed by averaging multiple perpendicular lines from the pia to the white matter in coronal MRI sections of V1.

Brain slice preparation

Electrophysiological experiments were conducted on brain slices of male Wistar rats (P26 - P36). The animals were deeply anesthetized by inhalation of isoflurane and decapitated. Brain slices (300 μ m) including V1, with reference to Paxinos and Watson (2007), were cut between 5 to 45 degrees to the coronal plane (to preserve the apical dendritic arbor of L5B pyramidal neurons, see Figure S1) in an ice-cold solution of composition (in mM): 125 NaCl, 25 NaHCO₃, 3 KCl, 1.25 NaH₂PO₄, 1 CaCl₂, 6 MgCl, 3 Na pyruvic acid and 25 glucose saturated with 95% O₂ and 5% CO₂. Slices were submerged in the same solution at 34°C for 15-30 minutes and then maintained at room temperature (20-25°C).

Whole-cell recordings

Individual slices were placed in a chamber perfused with a constant flow of artificial cerebrospinal fluid of composition (in mM): 125 NaCl, 25 NaHCO₃, 3 KCl, 1.25 NaH₂PO₄, 2 CaCl₂, 1 MgCl₂, 3 Na pyruvic acid and 25 glucose saturated with 95% O₂ and 5% CO₂ at 34-36°C. In the majority of experiments, spontaneous synaptic activity was blocked by the addition of CNQX (10 μ M, Tocris), DL-AP5 (50 μ M, Tocris), SR 95531 (5 μ M, Tocris), and CGP52432 (10 μ M, Tocris). In some experiments, ZD7288 (10 μ M, Tocris), TTX (1 μ M, Alomone), CsCl₂ (3 mM, Sigma), CdCl₂ (100 μ M, Sigma), and / or BaCl₂ (100 μ M, Sigma) were added to the extracellular solution. Recordings were made from thick-tufted L5 pyramidal neurons, identified by their large soma size, and thick apical dendrite projecting to layer 1, when visualized with video-enhanced infra-red differential interference contrast microscopy. Dual and triple whole-cell, current-clamp recordings were made with identical, dedicated current-clamp amplifiers (BVC 700A; Dagan). The electrode capacitance and series resistance were compensated using the active circuitry of the amplifier. Pipettes were filled with a solution containing (mM): 135 K-Gluconate, 7 NaCl, 10 HEPES, 2 Na₂ATP, 0.3 NaGTP, 2 MgCl, and 10 Na₂Phosphocreatine, pH 7.2 - 7.3, for somatic (open tip resistance 3-6 M Ω) or dendritic (open tip resistance 7-15 M Ω) recordings. In experiments where two electrodes were simultaneously used to make whole-cell patch-clamp recordings from closely spaced sites, one electrode was used to inject current and the other acted as a voltage follower. Somatic or dendritic recordings were rejected if the series resistance exceeded 20 or 50 M Ω , respectively. Signals were low-pass filtered (DC to 10 kHz) and acquired by Axograph software at 50 kHz. Experimental data were analyzed using Axograph, GraphPad Prism, SigmaPlot and Microsoft Excel. The recorded membrane potential values were adjusted for pipette offset, but not liquid junction potential.

In some experiments, simulated excitatory postsynaptic potentials were generated by the delivery of an excitatory postsynaptic current (EPSC)-shaped current waveform ($\tau_{\text{rise}} = 0.5$ ms, decay $\tau_{\text{decay}} = 5$ ms) or a series of pseudo-random barrages of EPSC-shaped waveforms delivered at somatic and dendritic sites (Williams, 2005). Barrages of pseudo-random (300 Hz bounded Poisson distribution) EPSC-shaped ideal current source ($\tau_{\text{rise}} = 0.5$ ms, decay $\tau_{\text{decay}} = 5$ ms) waveforms were formed by the linear addition of events generated by ten input sources with mean rates of between 10 and 200 Hz, which we describe as the input frequency. Conductance injection was achieved using a real-time dynamic clamp (SM1; Cambridge Conductance, 10%-90% settling time of 290 ns), using closely spaced (< 10 μ m) pipettes for voltage recording and current injection at dendritic sites. The characteristic of the excitatory conductance used were: Figure 4: AMPA component: $\tau_{\text{rise}} = 0.5$ ms, $\tau_{\text{decay}} = 5$ ms, NMDA component: $\tau_{\text{rise}} = 0.5$ ms, $\tau_{\text{decay}} = 150$ ms, AMPA:NMDA ratio 1:1, $E_{\text{rev}} = 10$ mV; Figure 8: AMPA component: $\tau_{\text{rise}} = 0.2$ ms, $\tau_{\text{decay}} = 2$ ms; NMDA component: $\tau_{\text{rise}} = 5$ ms, $\tau_{\text{decay}} = 150$ ms; AMPA:NMDA ratio 1:0.1; $E_{\text{rev}} = 10$ mV. Barrages of pseudo-random simulated dual-component AMPA and NMDA conductance waveforms were formed by the linear addition of events generated by input sources with mean rates of between 100 and 500 Hz (Williams, 2005). In all other experiments, ideal current steps of variable amplitude and duration were delivered to either the somatic or the dendritic electrode.

For glutamate iontophoresis experiments, a glass pipette (open tip resistance 50 M Ω) filled with L-glutamic acid (150 mM, pH = 7.0, monosodium salt) was positioned at a site close to (< 5 μ m) the apical dendritic recording electrode. A retention current (+3 to +20 nA) was constantly applied to the iontophoresis electrode. The amplitude of the retention current was adjusted to avoid any depolarization, or change in stability, of the dendritic membrane potential. Glutamate was iontophoretically ejected in response to short pulses (1 to 5 ms) of negative current (up to –200 nA). The iontophoretic ejection volume was estimated by retracting the iontophoresis pipette in 1 μ m increments (Figure S5).

Microscopy and neuronal reconstruction

For accurate reconstruction, neurons were filled with 0.5% biocytin (wt / vol, 5 mg / ml, Sigma) and slices fixed in 4% PFA (pH 7.3 – 7.4) for 12 hours. The slices were then reacted with 0.1% streptavidin conjugated with Alexa Fluor-488 or Alexa Fluor-568 (Invitrogen) and 0.1% Triton X-100 for 2 hours or overnight shaking at 4°C, and then mounted and coverslipped with Aqua Polymount (Polysciences Inc.). Optically sectioned (0.5 – 0.8 μ m z step size) x-y photomicrograph montages of neuronal morphology were acquired using an inverted spinning disk confocal microscope with a W1 Yokogawa spinning disk module (3i), Zeiss Axio Observer Z1 (Zeiss), Hamamatsu Flash4 sCMOS camera, and 40 \times 1.2 NA Plan-Apochromat water immersion objective. Photomicrographs were acquired using either 1 \times 1 or 2 \times 2 binning and one or two averages using Slidebook 6.0 software. An exposure of 100–900 ms was set to allow the greatest dynamic range for all processes while not being too long as to over-bleach the fluorophore. In some cases, slices were counterstained with DAPI or with immunolabeling of vGLUT-2 (Synaptic systems) in order to determine lamination and arealization of V1.

Neurons were manually reconstructed with Neurolucida (MicroBrightField) at high digital magnification, and the reconstructions were visualized and analyzed with Neurolucida Explorer (MicroBrightField) software. Neurons possessing dendritic arbors that appeared substantially truncated by the slicing procedure were excluded from further analysis. For illustrative purposes only, dendritic and axonal processes of reconstructions were thickened in Neurolucida Explorer and Adobe Illustrator in order to provide clarity in text figures.

For modeling studies, the morphology of each neuron was reconstructed from images subjected to deconvolution using the CMLE algorithm, with a signal-to-noise ratio of 40, with 60 iterations, using a measured point spread function (Huygens Professional version 17.04, Scientific Volume Imaging). To ensure the accuracy of images used for deconvolution, a quality check was performed using the diameter of thick, medium, and thin dendrites, and branch point diameter as test parameters. Deconvolved spinning disk (40 \times water, 1.2 NA objective) images were compared to deconvolved images obtained through a Zeiss LSM710 confocal microscope using a 63 \times oil objective (Plan-Apochromat 1.4 NA). Non-deconvolved spinning disk (40 \times) micrographs differed in measured diameter from LSM710 (63 \times) micrographs by + 24 \pm 8%, whereas deconvolved spinning disk images differed from deconvolved LSM710 images by only + 8 \pm 1%. For a dendrite of 1 μ m this equates to a 0.08 μ m difference.

Retrograde labeling

A subset of rats ($n = 4$) were deeply anaesthetized with isoflurane (2%–3%) and retrobeads (Red RetroBeads IX; Lumafluor) were injected unilaterally into the superior colliculi (200–1500 nl) with mineral oil-filled borosilicate glass pipettes attached to a nanoject II (Drummond). After at least 4 days recovery, brain slices were prepared, as detailed above. Neocortical neurons in V1 labeled with retrobeads were located exclusively in L5. Whole-cell patch-clamp recordings were made at the soma of retrolabeled neurons ($n = 20$ cells), and their morphology reconstructed and analyzed as detailed above.

Computational modeling and parameter fitting

Modeling was performed using the NEURON simulation environment v7.3 (Hines and Carnevale, 1997). Neuronal morphology was imported after reconstruction, with cell bodies imported as sets of 3D contours. This allowed the somatic compartment to approximate the volume and surface area of the contoured shape. Dendritic compartments were assumed to be cylindrical with a diameter as observed and reconstructed in the x-y plane. Experimental data were base-lined to 0 mV and the reversal potential of the leak conductance was set to 0 mV. Temperature was set at 35°C. Spines were not explicitly modeled but were incorporated by scaling specific membrane resistance (R_m) and specific membrane capacitance (C_m) to account for additional membrane surface area (Stuart and Spruston, 1998). A spine scale factor was calculated for each compartment based on spine densities measured in L5 thick tufted pyramidal neurons of the rat V1 (Larkman, 1991). An average spine area of 1.4 μ m² and density of 1.43 spines / μ m for basal dendrites, 6.3 for the apical trunk, 1.5 for oblique dendrites, and 0.91 for tuft dendrites was used. Spines were not modeled in the first 100 μ m of the apical trunk, and 20 μ m of basal dendrites, to account for observed aspiny regions.

Specific membrane resistance, specific membrane capacitance and axial resistivity were determined using a multiple parameter optimization technique employing the principal axis method for minimization of the square norm between the experimental and simulated curves (RegionFitness in NEURON (Hines and Carnevale, 1997)). The model was fit to experimentally recorded voltage perturbations generated in response to current steps. Recordings at the soma when current was injected through the same electrode were not included in the fitting procedure to avoid possible error attributable to incorrect bridge balancing. Specific membrane resistance was fit with a uniform distribution over the entire basal and apical dendritic tree or a non-uniform distribution, using a sigmoidal/Boltzmann function of the form:

$$Rm = Rm_{end} + (Rm_{start} - Rm_{end}) / (1 + \text{Exp}^{(distance - halfdistance)/slope})$$

Where R_{mend} and R_{mstart} depict the plateau regions of the sigmoidal curve, half-distance depicts the 50% point, distance is the path length along the dendrite, and slope is the slope of the function. R_{mend} , R_{mstart} , half-distance, and slope were all free parameters, to allow fit error minimization. For example, although R_{mend} and R_{mstart} define the maximum and minimum, they do not necessarily occur within the domain of the neuron and the entire length of dendrite may therefore have a sloped R_m . The slope parameter was lower bound to 50, as although lower values were found to sometimes improve the error, these improvements were minimal (Stuart and Spruston, 1998).

Simulations of associative integration in rostral and caudal V1 L5B pyramidal neurons were carried out on the passive models obtained after parameter fitting. The passive reversal potential was set to -68 mV, and a transient sodium (3000 pS / μm^2), fast (350 pS / μm^2) and slow potassium (700 pS / μm^2) conductance were inserted into the somatic compartment (conductances available on ModelDB). No dendritic voltage-gated conductance were present. Conductance densities were chosen to emulate the action potential firing rates observed experimentally. Excitatory post-synaptic current-shaped trains of ideal current, that exactly matched those used in experiments, were delivered to the nexus and/or soma. The somatic current injection amplitude was adjusted to evoke an action potential firing rate of 10 Hz. The dendritic current amplitude was not adjusted.

Experimental design

Electrophysiology experiments were repeated independently by both authors. Results from each experimenter did not differ and thus final data were pooled. No strategy for randomization and/or stratification was adopted. This study was not performed blinded. Inclusion and exclusion criteria for individual data types are detailed below.

QUANTIFICATION AND STATISTICAL ANALYSIS

Morphological quantification

For measurements, the nexus was defined as the major bifurcation of the apical trunk at the base of the apical tuft. Trunk length was measured as the path from soma to nexus. The average tuft length was measured as the average of the path length to all dendritic termini in the tuft from the nexus. Oblique dendrites were defined as any branch protruding from the apical trunk prior to the nexus. Dendritic field volumes were calculated from the 3D convex hull volume (Neurolucida Explorer), defined as the enclosed volume of the 3D convex polygon wrapping the dendritic tree, with vertices at the tip of the most distal dendrites. Average diameters were measured as the mean of the diameters of dendritic sections weighted by their length relative to the total length of the dendritic tree.

Statistical quantification and analysis

Values reported are mean \pm standard error of the mean (SEM), and n values represent the number of cells (individual n values are shown in the Results section and in figures). Coefficient of variation (CV) was calculated as standard deviation / mean. Statistical significance was defined as when the probability of the data being observed under a null hypothesis was less than an alpha level of 0.05. Data were subjected to a two-tail Students' t test or ANOVA unless otherwise stated. Welch's correction was used for samples with unequal variance. The Mann-Whitney test was used as a non-parametric test. Details of statistical tests can be found in the Results section. Statistical analysis was carried out using Prism 7 (Graphpad), and Sigmaplot 13 (SysStat Software).

MRI data was excluded if there were major deformations or damage observed in the brain. Morphological data were excluded if there were major truncation of dendritic processes obvious at the z axis border of the slice. Somatic or dendritic electrophysiological recordings were rejected if the series resistance exceeded 20 or 50 M Ω , respectively, if observed recordings were highly unstable, or if cells had a depolarized membrane potential relative to the norm. Simultaneous recordings were only included in analysis if apical dendritic recordings were established at sites greater than 85% of the length of the apical dendritic trunk. Modeled cells were excluded if they could not be adequately fit to experimental data determined by the experiments' judgement and/or by possessing a square norm error of fit substantially higher than the norm.

DATA AND SOFTWARE AVAILABILITY

Data and code is available upon request from the Lead Contact, Stephen Williams (srw@uq.edu.au).

Neuron, Volume 101

Supplemental Information

**Neocortical Topology Governs the Dendritic
Integrative Capacity of Layer 5 Pyramidal Neurons**

Lee N. Fletcher and Stephen R. Williams

Supplementary Information

Contains: 9 Supplementary Figures.

Figure S1. *Related to Figure 1*; Structural magnetic imaging demonstrates little gradient of neocortical thickness along the medial-lateral axis of the primary visual cortex (V1)

Figure S2. *Related to Figure 2*; Relationship between morphological features of layer 5B pyramidal neurons and rostro-caudal position in the primary visual cortex

Figure S3. *Related to Figure 2*; The diameter of layer 5B pyramidal neuron dendrites does not vary over the rostro-caudal axis of the primary visual cortex

Figure S4. *Related to Figure 3 and 5*; Dendritic recording site, voltage transfer, and apparent input resistance of rostral and caudal layer 5B pyramidal neurons

Figure S5. *Related to Figure 4*; Integration of dendritic excitatory input by rostral and caudal V1 L5B pyramidal neurons

Figure S6. *Related to Figure 6*; The effects of manipulating intracellular resistivity of modeled rostral and caudal V1 L5B pyramidal neurons

Figure S7. *Related to Figure 6*; The influence of the distribution of dendritic spines, and the diameter of neuronal processes on the specific membrane properties of model neurons

Figure S8 *Related to Figure 6*; Additive contributions of intracellular resistance and morphology to the electrotonic structure of rostral and caudal V1 L5B pyramidal neurons

Figure S9. *Related to Figure 8*; Associative integration in caudal L5B pyramidal neurons is replicated by a single active compartment model

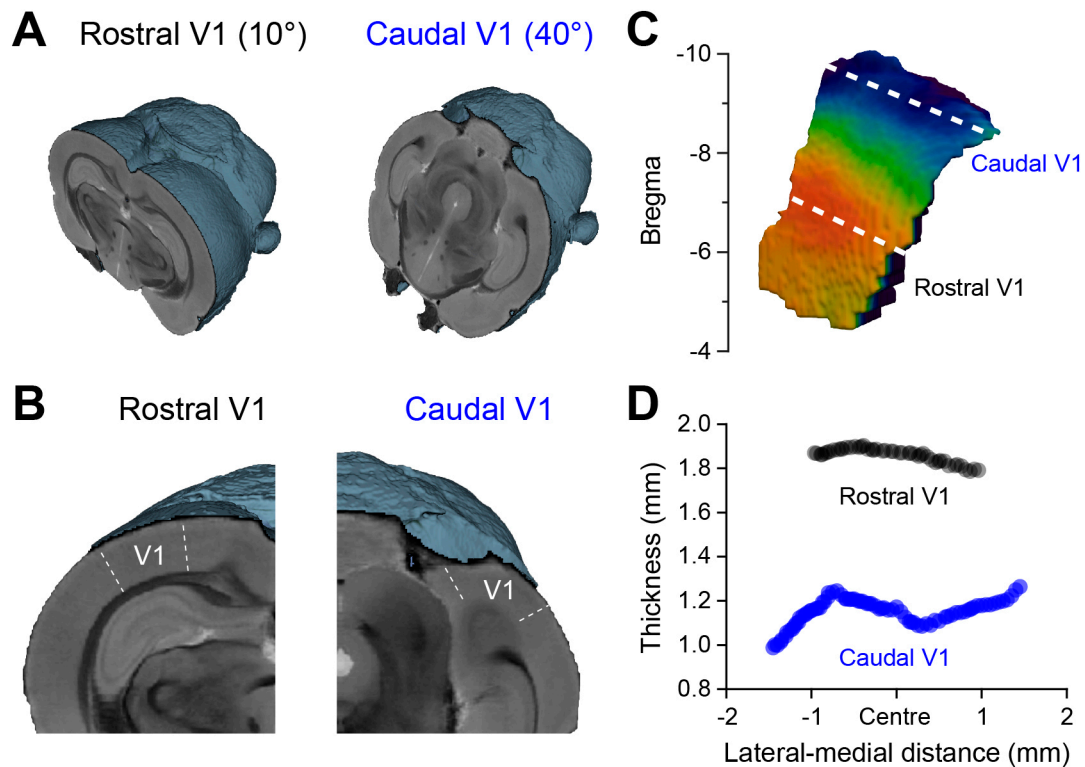


Figure S1. Related to Figure 1; Structural magnetic imaging demonstrates little gradient of neocortical thickness along the medial-lateral axis of the primary visual cortex (V1)

A, Virtual slicing of registered and averaged brain images at angles at which brain slices were prepared for electrophysiological recordings.

B, Higher magnification images illustrate the delineation of V1 in rostral and caudal sections.

C, Representation of V1 color coded by cortical thickness, the white dotted lines delineate the plane of analysis along the medial-lateral axis.

D, Average cortical thickness along the medial-lateral axis of rostral and caudal V1.

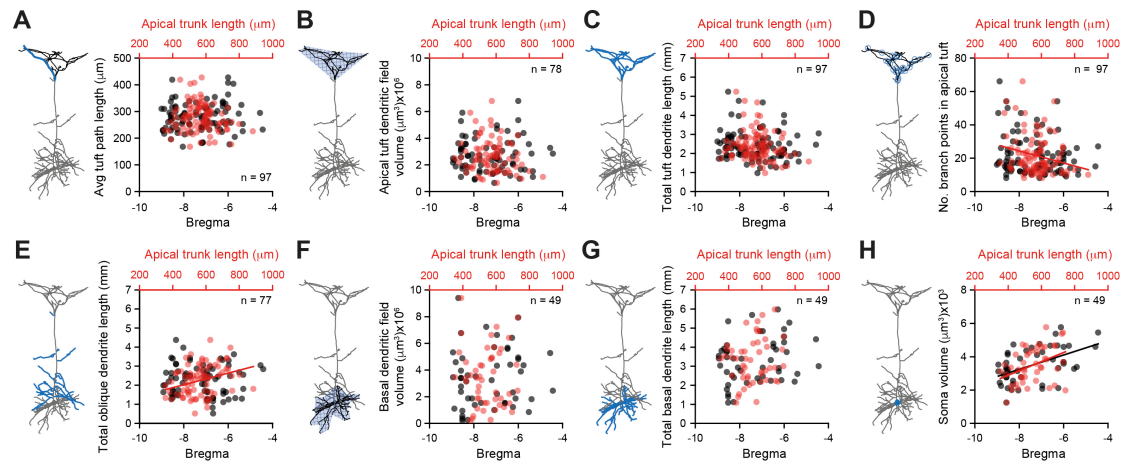


Figure S2. Related to Figure 2; Relationship between morphological features of layer 5B pyramidal neurons and rostro-caudal position in the primary visual cortex

The indicated morphological features are plotted with respect to bregma (black) and apical trunk length (red). Cartoons to the left illustrate the measurement parameter for each graph.

A, Average path length from the nexus (base of the apical dendritic tuft) to the termination of each apical dendritic tuft dendrite (linear regression with bregma: $F = 0.81$, $n = 97$, $P = 0.37$; with apical trunk length: $F = 1.78$, $P = 0.19$)

B, Apical tuft dendritic field volume calculated as the volume enclosed by a tight-fitting shape the vertices of which are at the outermost dendrites (see STAR Methods for detailed explanation) (linear regression with bregma: $F = 0.01$, $n = 78$, $P = 0.94$; with apical trunk length: $F = 2.36$, $P = 0.13$).

C, Total dendritic length of the apical dendritic tuft (linear regression with bregma: $F = 1.67$, $n = 97$, $P = 0.2$; with apical trunk length: $F = 3.2$, $P = 0.08$).

D, Total number of branch points in the apical dendritic tuft (linear regression with bregma: $F = 3.31$, $n = 97$, $P = 0.07$; with apical trunk length: slope = 2.7 branch points / 100 μm , $F = 5.1$, $r = 0.2$, $n = 97$, $P = 0.03$).

E, Total length of oblique dendrites, defined as all dendritic branches bifurcating from the apical dendritic trunk prior to the base of the apical dendritic tuft (linear regression with bregma: $F = 0.11$, $n = 77$, $P = 0.74$; with apical trunk length: slope = 4 μm / 100 μm , $F = 7.72$, $r = 0.31$, $n = 77$, $P = 0.01$).

F, Field volume of the basal dendritic tree (linear regression with bregma: $F = 0.57$, $n = 49$, $P = 0.46$; with apical trunk length: $F = 0.03$, $P = 0.86$).

G, Total length of basal dendrites (linear regression with bregma: $F = 3.38$, $n = 49$, $P = 0.07$; with apical trunk length: $F = 1.20$, $P = 0.28$).

H, Volume of the soma (linear regression with bregma: slope = $417 \pm 108 \mu\text{m}^3$ / mm of bregma, $r = 0.51$, $F = 14.9$, $n = 48$, $P = 0.0004$; with apical trunk length: slope = $387 \pm 140 \mu\text{m}^3$ / 100 μm , $F = 7.63$, $r = 0.38$, $P = 0.008$).

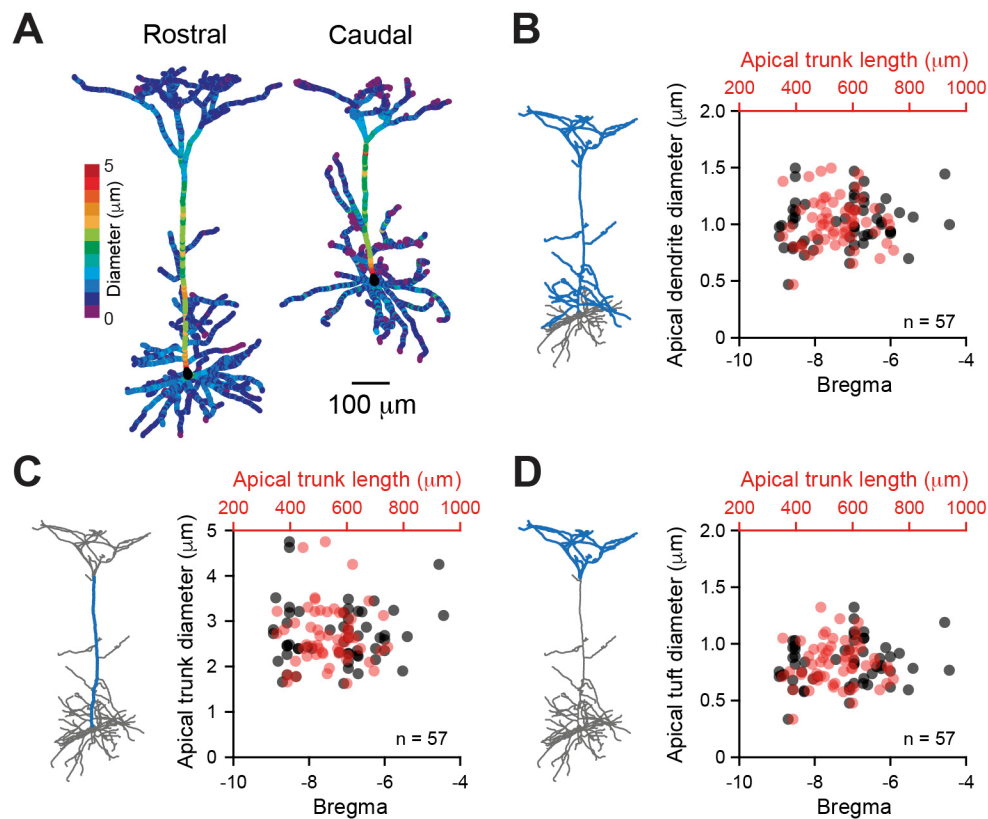


Figure S3. Related to Figure 2; The diameter of layer 5B pyramidal neuron dendrites does not vary over the rostro-caudal axis of the primary visual cortex

A, Examples of a rostral and a caudal V1 L5B pyramidal neuron colored coded by dendritic diameter.

B, The diameter of dendrites in the apical dendritic tree plotted with respect to bregma (black) and apical dendritic trunk length (red) (linear regression with bregma: $F = 1.67$, $n = 57$, $P = 0.20$; with apical trunk length: $F = 0.007$, $P = 0.94$). Cartoons to the left illustrate the measured sections of the dendritic tree.

C, The diameter of apical trunk dendrites (linear regression with bregma: $F = 0.14$, $n = 57$, $P = 0.71$; with apical trunk length: $F = 0.01$, $P = 0.91$).

D, The diameter of apical tuft dendrites (linear regression with bregma: $F = 1.71$, $n = 57$, $P = 0.20$; with apical trunk length: $F = 0.01$, $P = 0.92$).

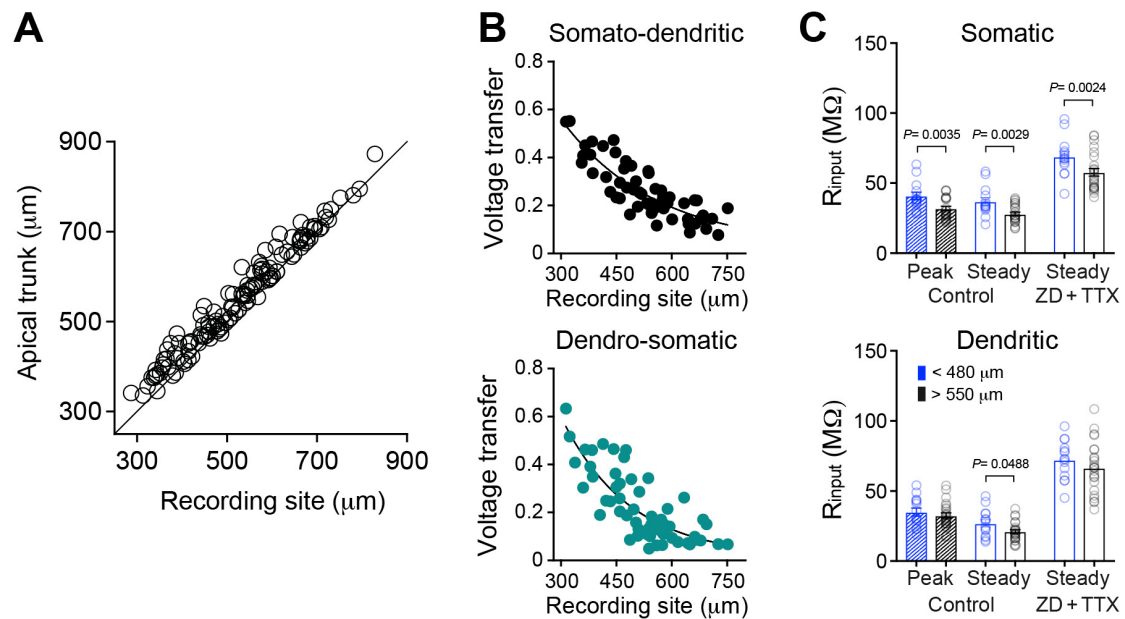


Figure S4. Related to Figure 3 and 5; Dendritic recording site, voltage transfer, and apparent input resistance of rostral and caudal layer 5B pyramidal neurons

A, Relationship between the site of apical dendritic recording and the length of the apical dendritic trunk ($n = 125$ simultaneous triple somato-dendritic whole-cell recordings; apical dendritic trunk length = $550.9 \pm 10.4 \mu\text{m}$; dendritic recording distance from soma = $527.1 \pm 10.9 \mu\text{m}$; $n = 125$. Dendritic electrode separation = $10.7 \pm 1.1 \mu\text{m}$). The line has a unity slope.

B, Somato-dendritic (upper graph, 50 % point = $330 \mu\text{m}$) and dendro-somatic (lower graph, 50 % point = $334 \mu\text{m}$) voltage transfer, in response to peak voltage excursions of $-19.9 \pm 0.1 \text{ mV}$ and $-20.1 \pm 0.1 \text{ mV}$ at the somatic (somatic current = $-0.76 \pm 0.03 \text{ nA}$) or dendritic (dendritic current = $-0.68 \pm 0.02 \text{ nA}$) recording site, respectively.

C, Peak (hatched bars) and steady-state (open bars) somatic (upper graph) and apical dendritic (lower graph) apparent input resistance of caudal (blue bars and symbols, apical trunk lengths $< 480 \mu\text{m}$) and rostral (black bars and symbols, apical trunk lengths $> 550 \mu\text{m}$) V1 L5B pyramidal neurons. Voltage responses were generated in response to small amplitude (-50 pA), long (800 ms) negative current steps under control and after the application of ZD7288 (ZD, $10 \mu\text{M}$) and TTX ($1 \mu\text{M}$). Note that somatic and dendritic values were recorded from the same neurons during simultaneous somato-dendritic recording. Bars represent mean \pm SEM. Statistical significance was tested with an unpaired T-test.

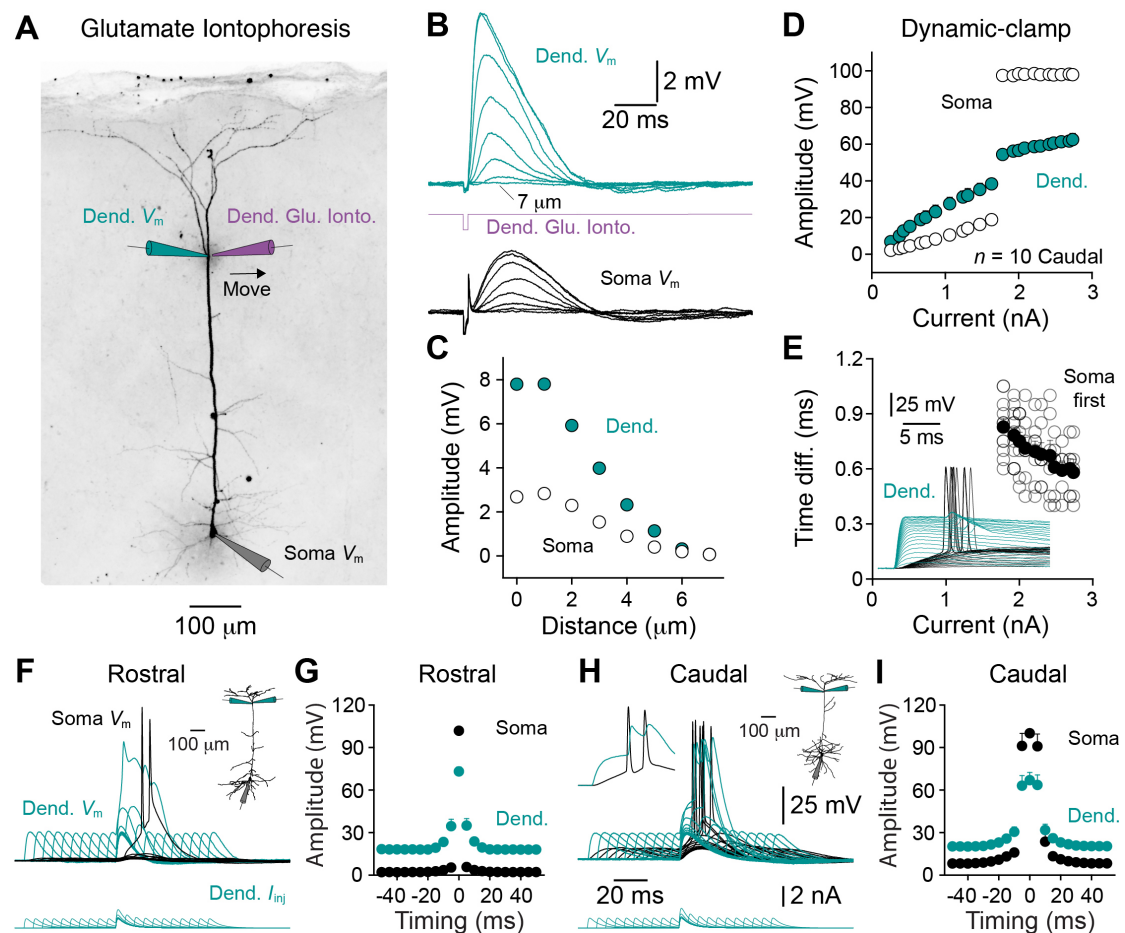


Figure S5. Related to Figure 4; Integration of dendritic excitatory input by rostral and caudal V1 L5B pyramidal neurons

A, Photomicrograph of a rostral V1 L5B pyramidal neuron showing the placement of recording and iontophoresis pipettes. The arrow shows the direction of movement of the iontophoresis pipette, which was retracted in one micrometer steps along the approach axis.

B, A family of simultaneously recorded voltage responses generated by the local dendritic iontophoretic application of glutamate. Note as the iontophoresis pipette was retracted in 1 μ m steps the amplitude of the voltage response decreases.

C, Relationship between the amplitude of voltage responses and the position of the iontophoresis pipette. Results in panels B and C were obtained from the neuron shown in panel A.

D, Threshold-aligned input-output relationship of caudal V1 pyramidal neurons generated in response to the injection of families of EPSC-shaped conductance changes using dendritic dynamic-clamp, conductance changes were composed of simulated AMPA and NMDA components. The discontinuity in these relationships delineates the threshold of action potential generation.

E, Action potentials were generated first and subsequently back-propagated to the site of dendritic recording in response to supra-threshold dendritic EPSC-shaped conductance changes in caudal V1 pyramidal neurons. The open symbols show the time disparity recorded in individual trials and the filled symbols the average. The inset overlain somatic and dendritic (Dend. V_m)

voltage responses show the absence of conductance-evoked dendritic spike generation and the sequence of action potential back-propagation.

F,H, Rostral (F) and caudal (H) V1 L5B pyramidal neurons show distinct modes and time-windows of synaptic integration. Simultaneous somatic (black traces) and apical dendritic (green traces) recording shows the summation of excitatory post-synaptic potentials (EPSPs) generated at distal dendritic sites in response to pairs of identical input injected as ideal current separated in time by 0 to ± 50 ms (5 ms steps) (rostral EPSC amplitude = 0.88 ± 0.06 nA, $n=9$; caudal EPSC amplitude = 1.12 ± 0.10 nA, $n=10$). In the rostral neuron, dendritic EPSPs evoked dendritic spike-driven action potential (AP) firing only when activated coincidently, whereas dendritic EPSPs in the caudal neuron directly evoked AP firing (inset).

G,I, Pooled data showing the average (\pm SEM) somatic (black) and dendritic (green) peak voltage response evoked by EPSPs generated at the indicated time intervals in rostral (G, $n=10$) and caudal (I, $n=9$) L5B pyramidal neurons.

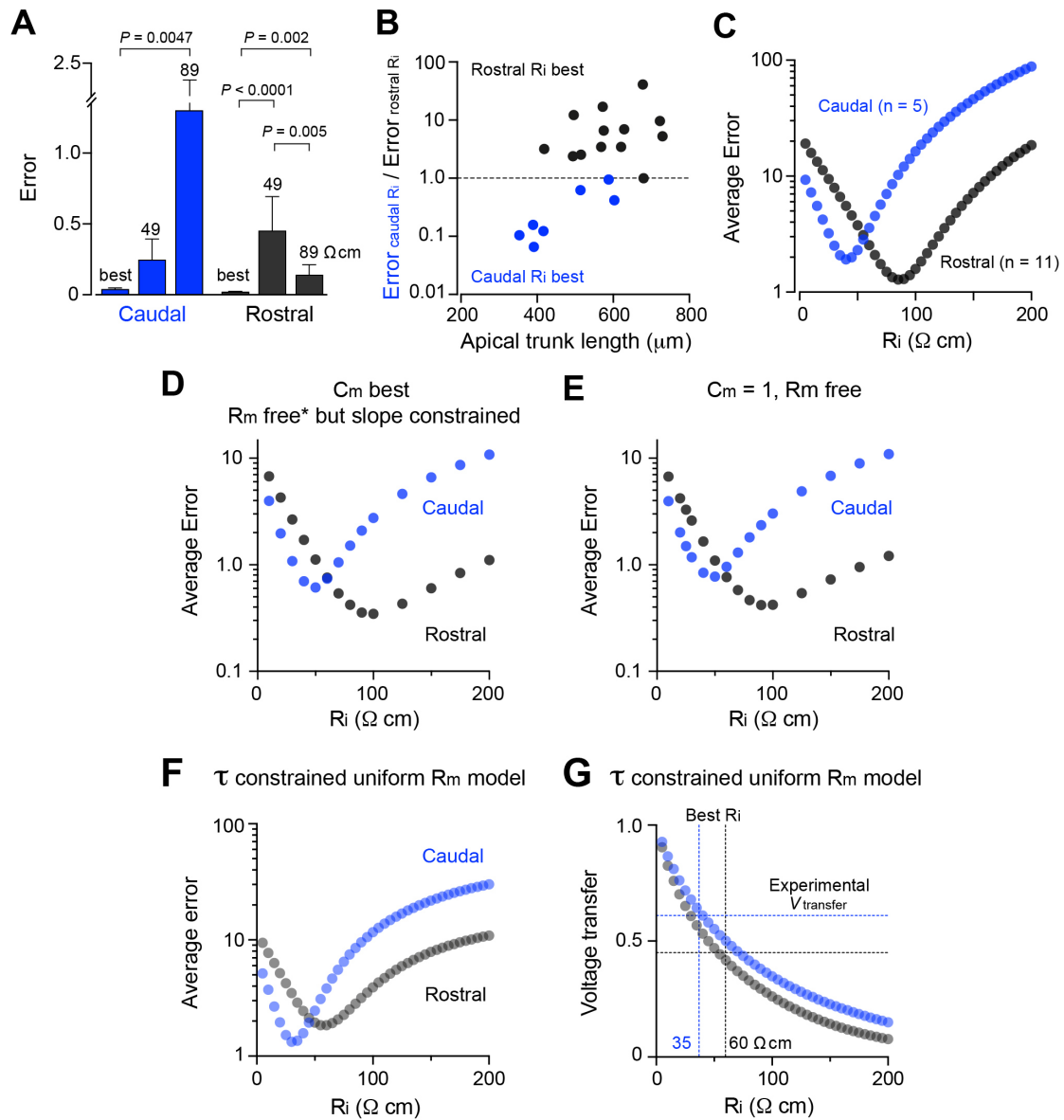


Figure S6. Related to Figure 6; The effects of manipulating intracellular resistivity of modeled rostral and caudal V1 L5B pyramidal neurons

A, The effects of manipulating the value of R_i determined for caudal (apical trunk length $<480 \mu$ m) and rostral (apical trunk length $>550 \mu$ m) modeled L5B pyramidal neurons. For caudal (blue) and rostral (black) neurons the mean total error between the experimental and model data is shown for the best fit value of R_i , the average value of R_i for each group, and that imposed by exchanging the average value of R_i between groups. Note the large increase in error when the average value of R_i was switched between groups (caudal neurons fit with $R_{i-rostral} = 89 \Omega$ cm: compared to best fit: mean ratio = 10.85 ± 0.21 , $P = 0.0047$; compared to $R_{i-caudal} = 49 \Omega$ cm; mean ratio = 4.62 ± 0.25 , $P = 0.043$) (rostral neurons fit with $R_{i-caudal} = 49 \Omega$ cm: compared to best fit: mean ratio = 15.7 ± 0.15 , $P < 0.0001$; compared to $R_{i-rostral} = 89 \Omega$ cm; mean ratio = 3.71 ± 0.13 , $P = 0.0018$). Significance was tested with a ratio paired T-test.

B, Relationship between apical dendritic trunk length and the ratio of the total error when neurons were fit with the average R_i of caudal neurons over the total error when fit with the average R_i of rostral neurons. Values less than 1 indicate

neurons are better fit with a $R_i = 49 \Omega \text{ cm}$ and values larger than 1 indicate neurons are best fit with a $R_i = 89 \Omega \text{ cm}$.

C, Mean error for a range of values of R_i (5 to 200 $\Omega \text{ cm}$, 5 $\Omega \text{ cm}$ steps) for caudal and rostral neurons.

D, Mean error for a range of values of R_i (10 to 200 $\Omega \text{ cm}$, 10 $\Omega \text{ cm}$ steps) for caudal and rostral neurons when the absolute values for R_m was free to be fit (R_m end was constrained to 1000 $\Omega \text{ cm}^2$ and the slope of the sigmoid function was constrained to a value of 50).

E, Mean error for a range of values of R_i (10 to 200 $\Omega \text{ cm}$, 10 $\Omega \text{ cm}$ steps) for caudal and rostral neurons when C_m was constrained to $1 \mu\text{F} / \text{cm}^2$ and R_m was a free variable to be fit.

F, The mean total error between simulation results and experimental data for a range of values of R_i when caudal and rostral neurons are fit to a uniform R_m model. The value of R_m was determined by the measured membrane time constant, with C_m constrained to $1 \mu\text{F} / \text{cm}^2$. Each point represents the average value obtained in 6 caudal and 11 rostral neurons (caudal $R_i = 35.7 \pm 4.9 \Omega \text{ cm}$, $n = 6$; rostral $R_i = 59.6 \pm 6.8 \Omega \text{ cm}$, $n = 11$; difference = 23.9 ± 9.96 , T-test, $P = 0.0298$).

G, Dendro-somatic voltage transfer for each value of R_i shown in panel E. Vertical dotted lines represent the average R_i for the best fit (minimum error) for caudal and rostral neurons. Horizontal dotted lines represent the mean of the experimentally measured dendro-somatic voltage transfer in these neurons.

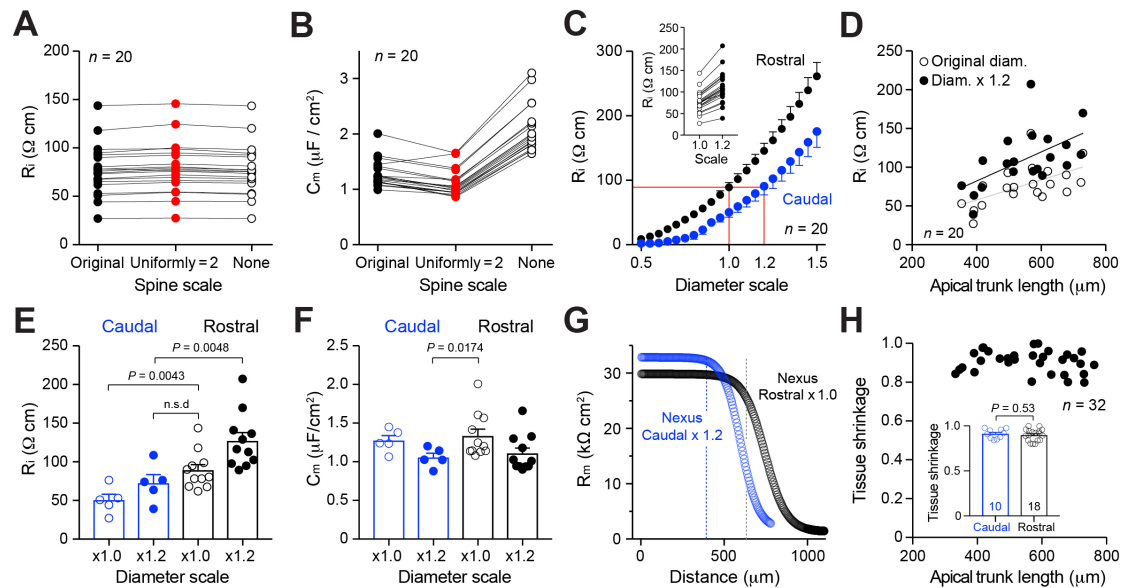


Figure S7. Related to Figure 6; The influence of the distribution of dendritic spines, and the diameter of neuronal processes on the specific membrane properties of model neurons

A-B, Values of specific intracellular resistivity (A, R_i) and membrane capacitance (B, C_m) when R_m and C_m were scaled to account for the increased membrane surface area imparted by dendritic spines. The original spine scale was dendritic compartment-dependent (filled black symbols, see Star Methods for details), whereas a uniform scale of 2 was applied to all spineous dendritic compartments (red symbols, uniformly=2). None refers to the omission of spine scaling (open symbols).

C, Values for R_i obtained when scaling the diameter of all compartments from 50% to 150% of the original value. R_m and C_m were constrained to the best fit values at the original diameter, but R_i was a free variable. Simulation results for caudal (blue, apical trunk length $<480 \mu m$, $n=5$) and rostral (black, apical trunk length $>550 \mu m$, $n=11$) L5B pyramidal neurons are shown. The R_i value of caudal neurons approached that of rostral neurons at a diameter scale of 1.2 (red solid lines). Direct fitting revealed that alteration of the diameter of each compartment altered the value of R_i obtained in simulations where R_i , R_m and C_m were free variables. The illustrated values in the inset represent those obtained at minimum error between model and experimental data when the diameter was scaled to 1.2.

D, Distribution of the best fit values of R_i at the original diameter (open circles) and when the diameter was scaled by 1.2 (filled circles) as a function of apical dendritic trunk length. Solid lines represent linear regression (R_i linear regression with apical trunk length: original diameter, slope= $130 \mu m / 100 \mu m$ of trunk length, $r=0.57$, $F=8.62$, $n=20$, $P=0.009$; diameter x1.2, slope= $187 \mu m / 100 \mu m$ of trunk length, $r=0.57$, $F=8.65$, $P=0.009$). Note the roughly parallel upward shift in the value of R_i with greater compartment diameter.

E, Scaling of the diameter by 1.2 preserves the differences between estimation of R_i in caudal ($n=5$) and rostral ($n=11$) L5B pyramidal neurons (T-test, original diameter, $P=0.0043$; T-test scaled diameter, $P=0.0048$). However, when caudal neurons were scaled by 1.2 and rostral neurons remained at their

original diameter no significant difference in the values of estimated R_i were apparent (T-test, n.s.d. (not significantly different), $P= 0.25$).

F, Scaling of the diameter by 1.2 altered the value of C_m estimated in both caudal and rostral groups. C_m was, however, significantly different in caudal neurons that were scaled by 1.2 compared with unscaled rostral neurons (caudal (diameter $\times 1.2$): $C_m=1.056 \pm 0.056 \mu\text{F}/\text{cm}^2$; rostral (diameter $\times 1.0$): $C_m= 1.334 \pm 0.087 \mu\text{F}/\text{cm}^2$, T-test, $P= 0.017$).

G, Average R_m distribution of caudal neurons diameter scaled by 1.2 and rostral neurons at their original diameter.

H, Direct measurement of tissue shrinkage in the x-y plane (calculated by the ratio of the distance between two points on the reconstructed neuron / distance on live image) as a function of trunk length. The inset shows average tissue shrinkage in caudal ($<480 \mu\text{m}$) and rostral ($>550 \mu\text{m}$) V1 (caudal= 0.91 ± 0.02 , $n = 10$; rostral= 0.90 ± 0.02 , $n = 18$; unpaired T-test, $P= 0.533$).

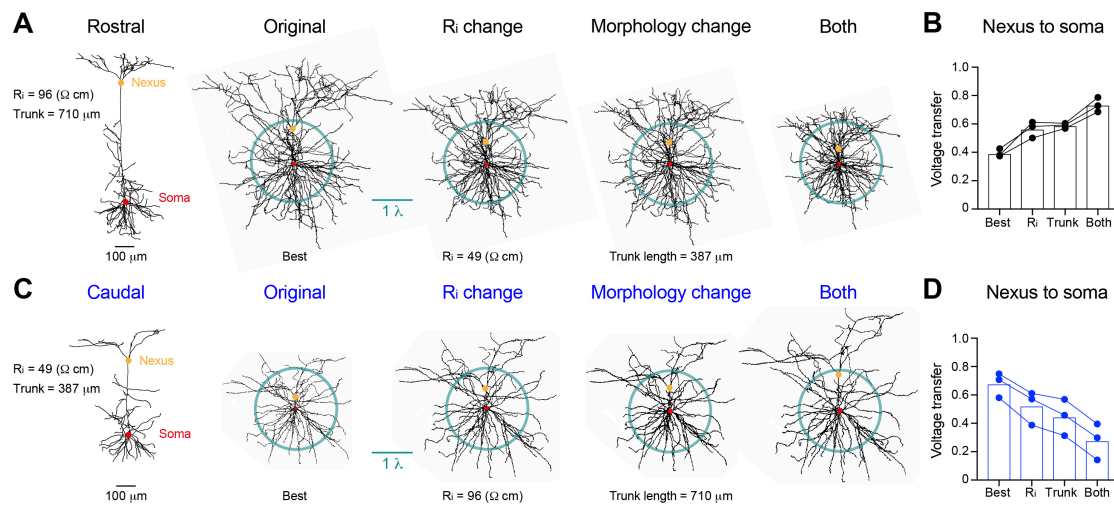


Figure S8 Related to Figure 6; Additive contributions of intracellular resistance and morphology to the electrotonic structure of rostral and caudal V1 L5B pyramidal neurons

A, Morphology of a rostral L5B pyramidal neuron (left image), which was transformed into a morphoelectrotonic representation, using best fit values of intracellular resistance (R_i , best), when R_i was changed to a lower value (R_i change, value equals the caudal average in panel C), and when the morphology was altered by removing a section of the apical dendritic trunk (morphology change), or when both values of R_i and morphology were altered (both). In each morphoelectrotonic transform, the radius of the blue circle indicates one length constant (λ), and the positions of the soma (red point) and the base of the apical dendritic tuft (orange point) are indicated. Note, that both a reduction of R_i and the pruning of the apical dendritic trunk were required to sculpt morphoelectrotonic transforms to resemble the illustrated caudal neuron (panel C, original).

B, Dendro-somatic voltage transfer from the base of the apical dendritic tuft (nexus) to the soma of rostral neurons following the indicated manipulations. The values for R_i and apical dendritic trunk length presented are averages of the 3 rostral neurons used for this analysis.

C, The effects of the addition of apical dendritic trunk length and increased R_i on the morphoelectrotonic representation of a caudal L5B pyramidal neuron. Note that morphoelectrotonic transform of the caudal neuron resembled that of the rostral L5B pyramidal neuron (original, panel A), when R_i was increased (R_i change, value equals rostral average in panel A) and a section of apical dendritic trunk inserted (synthetic trunk length equal average of rostral neurons, shown in panel A).

D, Dendro-somatic voltage transfer from the base of the apical dendritic tuft (nexus) to the soma following the indicated manipulations in caudal neurons. The values for R_i and apical dendritic trunk length presented are averages of the 3 caudal neurons used for this analysis.

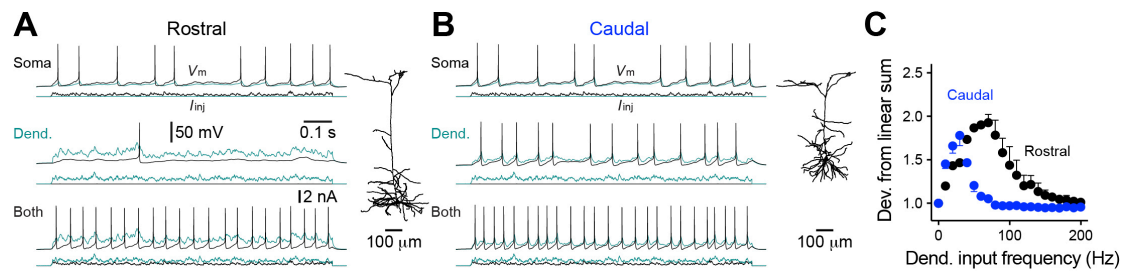


Figure S9. Related to Figure 8; Associative integration in caudal L5B pyramidal neurons is replicated by a single active compartment model

A-B, Simulation of action potential (AP) firing in rostral (A) and caudal (B) L5B pyramidal neurons. In each simulation sodium and potassium conductances were inserted exclusively in the somatic compartment. Note that low frequency repetitive AP firing with rates matching those experimentally observed was generated in response to somatically delivered barrages of EPSPs, with properties identical to those used experimentally. In contrast, barrages of excitatory input delivered to the nexus of the apical dendrite evoked contrasting AP firing rates. In the caudal model the rate and pattern of AP firing replicated those observed experimentally. The lower panels show that the associative integration of somatic and dendritic input produced AP output with properties that replicated experimental observation in the caudal, but not the rostral modeled neuron.

C, AP firing generated by associative integration deviated from the linear summation of the AP output generated by somatic and dendritic input alone in a characteristic manner in caudal and rostral modelled neurons. Note that the early peaked relationship in the caudal neurons replicated experimental observations. In contrast, in models of rostral neurons the relationship evolved to a peak at higher dendritic input frequencies, and in contrast to experimental observations declined as the dendritic input frequency increased further.